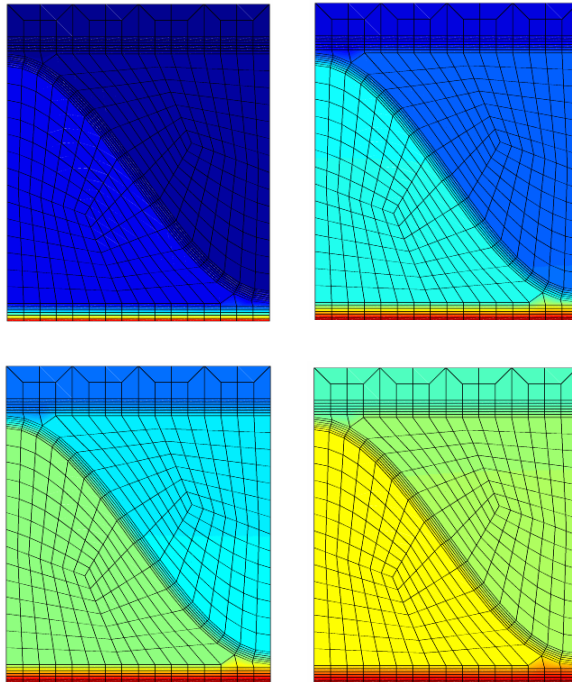




LUND
UNIVERSITY



MOISTURE DYNAMICS IN CORRUGATED BOARD BOXES

HENRIK LYNGÅ and GUSTAV SIKÖ

Structural
Mechanics

Master's Dissertation

Structural Mechanics

ISRN LUTVDG/TVSM--03/5120--SE (1-80)

ISSN 0281-6679

MOISTURE DYNAMICS IN CORRUGATED BOARD BOXES

Master's Dissertation by
Henrik Lyngå and Gustav Sikö

Supervisors:

Ulf Nyman and Per Johan Gustafsson,
Div. of Structural Mechanics, Lund
Tomas Nordstrand and Rickard Hägglund,
SCA Research, Sundsvall

Copyright © 2003 by Structural Mechanics, LTH, Sweden.
Printed by KFS I Lund AB, Lund, Sweden, June 2003.

For information, address:
Division of Structural Mechanics, LTH, Lund University, Box 118, SE-221 00 Lund, Sweden.
Homepage: <http://www.byggmek.lth.se>

Abstract

In this master thesis a two-dimensional finite element model describing nonlinear moisture dynamics in paper materials is developed. The aim of the model is to simulate moisture movement in corrugated board boxes due to fluctuating relative humidity.

To evaluate the accuracy of the model a simulation is carried out which is being compared to measurements. For the paper material used in the simulation adsorption and desorption characteristics are experimentally determined.

Keywords: FEM, finite element analysis, two-phase model, corrugated board, moisture dynamics, hysteresis, sorption

Acknowledgements

This master's thesis was completed during the spring 2003 at the Division of Structural Mechanics, Lund University, Sweden in cooperation with SCA Research, Sundsvall.

First of all we would like to express our gratitude to our supervisors Lic. Eng. Ulf Nyman and Prof. Per Johan Gustafsson at the Division of Structural Mechanics, Lund University and to Dr. Tomas Nordstrand and Lic. Eng. Rickard Hägglund at SCA Research, Sundsvall.

We would like to thank the staff at the Division of Structural Mechanics for being such nice fellows, Bo Zadig for his help finishing the report and specially technician Thord Lundgren for helping us out during measurements performed at the Division of Structural Mechanics. We are also very grateful to Dr. Eberhard Lehmann, Peter Vonthobel and Gabriel Frei at the Paul Scherrer Institute (PSI), Switzerland, who helped us out during the experiments at NEUTRA.

Lund, June 2003

Henrik Lyngå Gustav Sikö

Summary

A method to simulate moisture dynamics in corrugated board boxes by finite element analysis is developed. Controlling the moisture characteristics when analyzing strength properties in the design process is of great demand. This is due to the material properties being very sensitive to the level of moisture concentration and the moisture gradient induced causes shape-instability which may reduce the strength.

The transport model is based on mass conservation for a mixture containing a vapor phase and an adsorbed liquid phase. The phases are represented as vapor density in the pores ρ_v [kg/m^3] and moisture concentration in the fibres c_l [kg/kg]. Three phenomena governing the moisture transport are taken into account.

- The transport is governed by Fick's diffusion law and occurs only in the vapor phase.
- The liner's surface outside the box is subjected to a convective boundary layer.
- The mass transfer between the two phases is governed by the sorption characteristics of the material.

The boundary adsorption and desorption curves (figure 1) are obtained in experiments and the hysteresis effect is dealt with using a higher order sorption law.

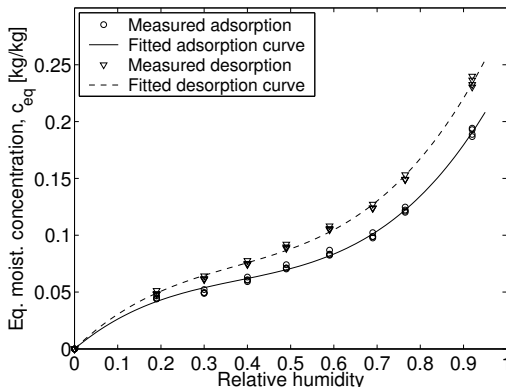


Figure 1: Boundary adsorption and desorption curves

Isoparametric finite element equations in the two-dimensional case are derived by linearizing the equations describing the transport and approximating them by 2×2 gauss integration. A combined Newton-Raphson and Euler backward method is used in the iterative process for convergence towards numerical equilibrium of the nodal values. For verification of the numerical implementation, vapor density profiles obtained in a two-dimensional, a one-dimensional and an analytical solution of a simple case are compared. The solutions all yield the same result.

Simulations, based on climate data measurements of relative humidity RH and temperature T outside and inside of a box, placed in an unheated shelter, are performed for a period of one month. The result of the FE-model resembles the measured RH inside the box.

The result of the two-dimensional simulation for six days in the beginning of June is shown in figure 2.

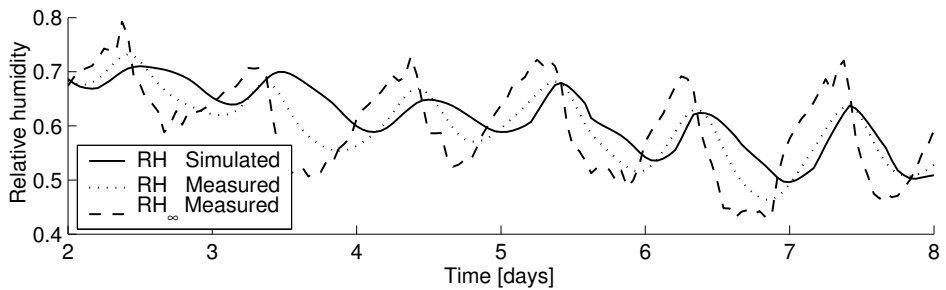


Figure 2: Simulation of relative humidity inside the box due to fluctuating external climate. RH_{∞} is the relative humidity outside the box

Sammanfattning

Syftet med examensarbetet är att utveckla en metod att simulera fuktdynamik med finita element i wellpappkartonger. Det finns ett behov av att integrera fukts inverkan i hållfasthetsanalyser eftersom fukthalten kraftigt påverkar egenskaperna hos pappersmaterial och eftersom fuktgradienten ger utböjning och därmed minskad bärförmåga.

Fukttransportmodellen är baserad på massbalans hos ett tvåfasssystem bestående av en ångfas och en vätskefas där vattnet är bundet i fiberna. Ångfasen representeras som ångdensitet i porerna ρ_v [kg/m^3] och vätskefasen som fuktkvot i fiberna c_l [kg/kg]. I modellen tas hänsyn till tre olika fenomen.

- Transporten styrs av Fick's lag och sker i ångfasen medan vätskefasen fungerar som en buffert. Diffusiviteten i Fick's lag antas vara isotrop.
- Papperets yta antas fungera som ett konvektivt skikt och flödet styrs av skillnaden i ånghalt mellan ytan och omgivande luft.
- Massutbytet mellan de två faserna styrs av materialets sorptionsegenskaper.

Adsorptions- och desorptionskurvor (figur 3) är framtagna i experiment och hystereseffekten som ger upphov till inre sorptionskurvor beskrivs med en modell.

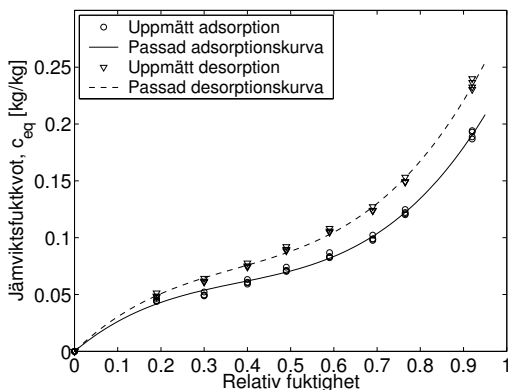


Figure 3: Sorptionskurvor för adsorption respektive desorption

Genom linearisering och FE-approximering av ekvationerna som styr transporten samt integrering med 2×2 gausspunkter erhålls tvådimensionella isoparametriska 4-nodselement. Newton-Raphsonmetoden i kombination med jämviktsutvärdering enligt Euler-baklänges används i den iterativa processen för att erhålla numerisk jämvikt hos nodvariablerna. För att verifiera implementeringen jämförs resultaten av FE-simuleringar i en respektive två dimensioner med den analytiska lösningen i form av ånghaltsprofiler. Överensstämmelsen är god.

Simuleringar, baserade på uppmätta klimatdata i form av relativ luftfuktighet RH och temperatur T på utsidan och insidan av en wellpappkartong placerad i en ouppvärmad lagerlokal, genomförs för juni månad. Resultaten visar på att FE-modellen överensstämmer med de uppmätta värdena av RH inne i lådan. Resultatet av tvådimensionell simulering för sex dygn i början av juni visas i figur 4.

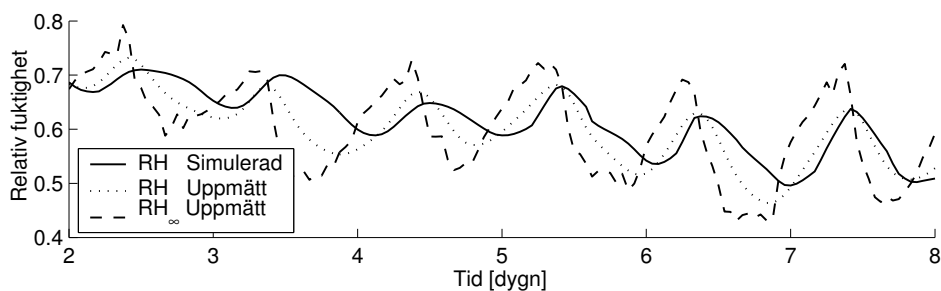


Figure 4: Simulering av relativ fuktighet inne i wellpappkartong. RH_∞ är relativ fuktighet utanför lådan

Contents

1	Introduction	1
1.1	Background	1
1.2	Aim and scope of the thesis	2
1.3	Formulation of the problem	2
1.4	Procedure of solving the problem	3
2	Theory	4
2.1	Transport model	4
2.2	Hysteresis	6
3	Experimental study of sorption in paper	10
3.1	Method	10
3.2	Result	10
4	Numerical formulation	12
4.1	Derivation of element equations	12
4.1.1	Strong form	12
4.1.2	Weak form	13
4.1.3	Finite element formulation	15
4.1.4	Paper element	16
4.1.5	Air element	18
4.1.6	Gauss integration	20
4.2	Computing implementation	22
4.2.1	Time integration	22
4.2.2	Schematic program	23
4.3	Verification	24
5	Finite element analysis	25
5.1	Geometry	25
5.2	Boundary conditions	25
5.3	Material modelling	26
5.4	Introductory simulations	28
5.5	Climate measurements	30
5.6	Simulations	31

6	Neutron radiography	36
6.1	Summary	36
6.2	NEUTRA	36
6.3	Description of the tests	38
6.3.1	Test A	39
6.3.2	Test B	39
6.3.3	Test C	39
6.3.4	Test D	41
7	Concluding remarks	46
7.1	Conclusions	46
7.2	Possible improvements of the model	46
	Bibliography	47
	Appendices	48
A	Sorption, numerical values	48
B	Verification of the numerical formulation	50
B.1	Analytical versus one-dimensional	50
B.2	One-dimensional versus two-dimensional	51
C	Analytical solution	53
D	Element functions	58

Chapter 1

Introduction

1.1 Background

The use of corrugated board is widely spread and is included in many different applications. Production of corrugated board boxes for storage use is one of the most important business within this field and there is a constant need for optimization of such packaging systems. Much effort is put in research in order to analyze material properties, such as strength and durability, because corrugated board is likely to retain its popularity in the future and has numerous advantages compared to other packaging materials. Some of them are [1]:

- + Low weight. Saves resources when transporting.
- + Can be entirely customized for specific purposes.
- + It is strong and stiff compared to its weight.
- + Easy to handle.
- + Easy to print.
- + Fully recyclable.

However, an important disadvantage is the strength and stability of the material being very sensitive to humidity. The level and duration of moisture content play a significant role for failure criteria. Due to hygroexpansion the moisture gradient induced causes shape-instability which may reduce the strength. Therefore, there is a need for taking the moisture distribution into account in the design process.

1.2 Aim and scope of the thesis

By storage and transportation corrugated board boxes are subjected to fluctuating and often high levels of relative humidity RH . This will of course effect the moisture content of the material, which has a significant influence on the strength of the boxes. Connecting the moisture content to the design process would certainly improve the accuracy while simulating collapse or other behavior of the board.

On behalf of SCA Research the intention with this master thesis is to provide tools for analyzing transient moisture dynamics in boxes due to external climate influence.

1.3 Formulation of the problem

The task is to implement a finite element model in order analyze moisture transport in paper materials and verify the model by simulating transient moisture dynamics in corrugated board boxes and comparing to measurements. The model is implemented using two-dimensional isoparametric elements.

1.4 Procedure of solving the problem

The commercial numerical software MATLAB is used in the computational work. The procedure of solving the present task can be summarized in the following order:

- Definition of equations describing a two-phase moisture transport model consisting of a vapor phase and an adsorbed water phase.
- Obtaining equilibrium sorption quantities from experiments performed at the division of Structural Mechanics at Lund University.
- Linearizing the equations and approximating finite element equations in the two-dimensional case that can be solved using backward Euler time integration.
- Verification of the numerical implementation by comparing to the analytic solution for a simple case.
- Verification of the transport model by comparing to moisture concentration profiles obtained in experiments using neutron radiography performed at the Paul Sherrer Institute (PSI), Switzerland, see chapter 6. However, it turned out that this part of the verification was not possible to carry out.
- Simulation of moisture dynamics in corrugated board boxes subjected to fluctuating external climate and comparing to measurements from experimental studies performed under unheated conditions in a barn in Asa, Våxjö.

Chapter 2

Theory

2.1 Transport model

The transport model is based on mass conservation for a mixture containing a vapor phase and an adsorbed water phase. In a model given by Ramarao [5] three resistances to mass transfer in the sorption process are introduced. The first is a surface resistance existing at the paper sheet's surface caused by a boundary layer resisting vapor diffusion from the bulk air to the sheet's surface. The second resistance is manifested in the vapor phase, i.e. diffusion inside the void spaces of the sheet. The third is the diffusive resistance to moisture movement in the interior of the fibres. This bound water diffusion is, compared to the diffusion in the void space, very slow and is thereby neglected here. However, the bound water phase will serve as a reservoir and a mass exchange with the vapor phase is dealt with.

The derivation of the physical model of moisture transport in the present studies is done for the one dimensional case in the region $0 < x < L$ with a convective boundary layer at $x=L$.

The flux Φ [$\text{kg}/\text{m}^2\text{s}$] of free vapor diffusion in air is described by Fick's law

$$\Phi = -D_a \frac{\partial \rho_v}{\partial x} \quad [\text{kg}/\text{m}^2\text{s}] \quad (2.1)$$

where D_a [m^2/s] is the vapor diffusivity in air and ρ_v [kg/m^3] the vapor density.

When diffusion occurs in a porous medium, such as paper, the diffusivity will be reduced due to the extended transportation path. The porosity must be taken into account since we define Φ and ρ_v in the pores and this leads to following expression.

$$\varepsilon \Phi = -D_v \frac{\partial \rho_v}{\partial x} \quad [\text{kg}/\text{m}^2\text{s}] \quad (2.2)$$

where ε ($0 \leq \varepsilon \leq 1$) is the porosity and D_v [m^2/s] the diffusivity in the void system.

The spatial derivative of the flux measures the rate of density decrease according to

$$\dot{\rho}_v = -\frac{\partial \Phi}{\partial x} \quad [\text{kg}/\text{m}^3\text{s}] \quad (2.3)$$

Combining (2.2) and (2.3) results in

$$\varepsilon \dot{\rho}_v = D_v \frac{\partial^2 \rho_v}{\partial x^2} \quad [kg/m^3 s] \quad (2.4)$$

If the moisture concentration in the fibre phase is not in equilibrium with the vapor density in the pores a mass transfer will occur between these phases according to

$$\dot{c}_l = k_c (c_{eq}(\rho_v) - c_l) \quad [1/s] \quad (2.5)$$

where c_l denotes the actual moisture concentration defined as the ratio between bound water density and dry sheet density $\frac{\rho_l}{\rho_s}$. c_{eq} is the equilibrium moisture concentration, depending on ρ_v and the temperature T . k_c [1/s] is the interface mass transfer coefficient.

Adding this to (2.4) gives

$$\varepsilon \dot{\rho}_v + \rho_s \dot{c}_l = D_v \frac{\partial^2 \rho_v}{\partial x^2} \quad [kg/m^3 s] \quad (2.6)$$

where ρ_s [kg/m³] is the dry sheet density.

The mass flux $\Phi_n = D_v \frac{\partial \rho_v}{\partial x} \Big|_{x=L}$ out of the paper surface is governed by the difference between the vapor density in the air $\rho_{v,\infty}$ and at the surface $\rho_{v,x=L}$ and the convective boundary coefficient k_b [m/s] according to

$$D_v \frac{\partial \rho_v}{\partial x} \Big|_{x=L} = k_b [\rho_{v,\infty} - \rho_{v,x=L}] \quad [kg/m^2 s] \quad (2.7)$$

These three equations (2.5)-(2.7) together describe the transport model in the one dimensional case.

Formulation of the equations for describing a 3-d region Ω with the convective boundary $\partial\Omega$ is needed for subsequent numerical formulations. Derivation of them are excluded as similarity to the 1-d equations is obvious.

$$\dot{c}_l = k_c (c_{eq}(\rho_v) - c_l) \quad [1/s] \quad (2.8)$$

$$\varepsilon \dot{\rho}_v + \rho_s \dot{c}_l = \nabla^T \cdot (D_v \mathbf{I} \nabla \rho_v) \quad [kg/m^3 s] \quad (2.9)$$

$$(D_v \mathbf{I} \nabla \rho_v)^T \cdot \mathbf{n} = k_b (\rho_{v,\infty} - \rho_{v,\partial\Omega}) \quad [kg/m^2 s] \quad (2.10)$$

where \mathbf{n} is the unit exterior normal vector at $\partial\Omega$. The nabla operator ∇ is defined as

$$\nabla = \begin{bmatrix} \frac{\partial}{\partial x} \\ \frac{\partial}{\partial y} \\ \frac{\partial}{\partial z} \end{bmatrix}$$

\mathbf{I} is the unit matrix and $D_v \mathbf{I}$ expresses isotropic vapor diffusivity in the material. Looking at figure 2.1 orthotropic properties might be more appropriate but measurements in order to define D_v are performed only in the x-direction, which also is the main transport direction. Therefore D_v is assumed to hold for as well the machine direction (MD) and the cross direction (CD).

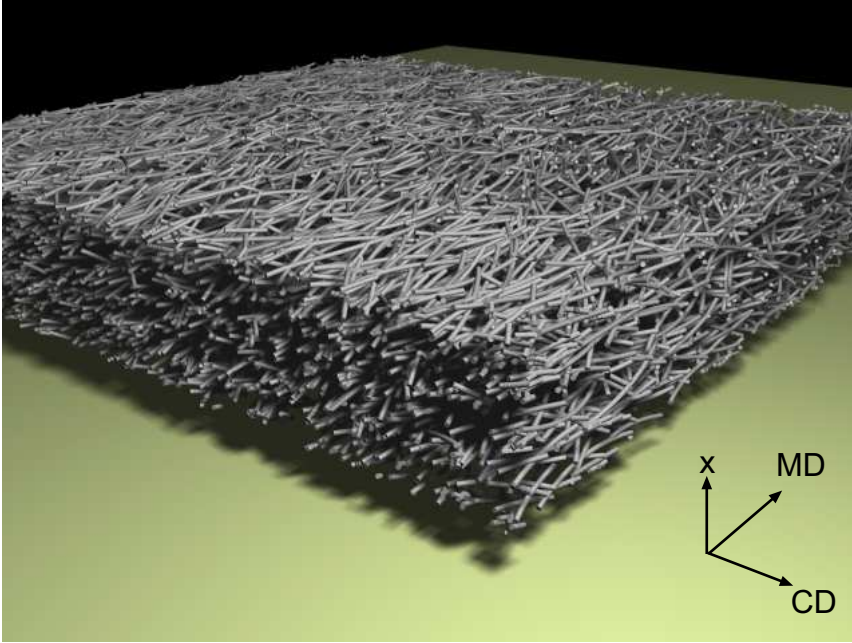


Figure 2.1: Fibre structure [2]

2.2 Hysteresis

An initially dry porous material which under a long time is subjected to a certain relative humidity RH will after reaching equilibrium achieve the moisture concentration $c_{eq}(RH)$. If this equilibrium state is reached during moisture uptake it will follow the adsorption curve, $c_{eq}^{ads}(RH)$.

On the other hand, if c_{eq} is evaluated while drying from fully soaked conditions the equilibrium moisture concentration will follow the desorption curve, $c_{eq}^{des}(RH)$.

The adsorption and desorption curves differ from each other and describe the lower and the upper limits of a possible interior sorption path, $c_{eq}^{int}(RH)$. This is due to the hysteresis effect.

Hysteresis is manifested in a branch switch of the equilibrium sorption path due to change in direction of evolution of relative humidity.

The development of higher order hysteresis curves due to fluctuating relative humidity is a complex phenomena and will depend on the history of the sorption path. This history dependent path can be tracked by the use of a set of discrete memory variables, $\kappa = \{\kappa_1, \kappa_2, \dots\}$ showing the direction of the sorption process during history of time intervals $t = \{t_0 \leq t \leq t_1, t_1 \leq t \leq t_2, \dots\}$. $\kappa = 1$ for adsorption and $\kappa = -1$ for desorption. This means that the sorption equilibrium is a function of RH , κ , K_a and K_d .

$$c_{eq} = f(RH, \kappa, K_a, K_d)$$

where K_a and K_d are defined as the initial slopes of a new path at the reversal point relative to the previous path, whenever the sorption process changes direction, from desorption to adsorption or from adsorption to desorption.

The boundary sorption curves as well as interior sorption paths are approximated by polynomials of third degree according to

$$c_{eq}(RH) = \alpha RH + \beta RH^2 + \gamma RH^3 \quad (2.11)$$

c_{eq}^{ads} and c_{eq}^{des} are obtained in experiments described in chapter 3 whereas c_{eq}^{int} is constituted using a model developed by Nyman [4].

First of all a set of equilibrium sorption paths corresponding to a set of time intervals is defined.

$${}^t c_{eq} \quad \text{for } t = \{t_0 \leq t \leq t_1, t_1 \leq t \leq t_2, \dots\} \quad (2.12)$$

The sorption path at each time interval can be either of c_{eq}^{ads} , c_{eq}^{des} or c_{eq}^{int} .

Given the sorption path at a previous time step ${}^{t-\Delta t} c_{eq}$ the sorption path ${}^t c_{eq}$ for next time step is defined as follows.

If the state of adsorption or desorption is maintained, κ does not change sign (${}^t \kappa = {}^{t-\Delta t} \kappa$) and the sorption path is identical to the previous path.

$${}^t c_{eq} = {}^{t-\Delta t} c_{eq} \quad (2.13)$$

If the sorption process changes direction from adsorption to desorption (${}^{t-\Delta t} \kappa = 1$, ${}^t \kappa = -1$) secondary or higher order interior sorption path c_{eq}^{int} develops according to following conditions.

$$\begin{aligned} \left. \frac{dc_{eq}^{int}}{dRH} \right|_{RH=t-\Delta t RH} &= K_d \left. \frac{d{}^{t-\Delta t} c_{eq}}{dRH} \right|_{RH=t-\Delta t RH} \\ \left. \frac{dc_{eq}^{int}}{dRH} \right|_{RH=RH_b} &= \left. \frac{dc_{eq}^{des}}{dRH} \right|_{RH=RH_b} \quad RH_b < {}^{t-\Delta t} RH \\ c_{eq}^{int}({}^{t-\Delta t} RH) &= {}^{t-\Delta t} c_{eq}({}^{t-\Delta t} RH) \\ c_{eq}^{int}(RH_b) &= c_{eq}^{des}(RH_b) \end{aligned}$$

where RH_b is the junction point of interior sorption path and boundary desorption curve. The new sorption path is described by

$${}^t c_{eq} = c_{eq}^{int} \quad (RH > RH_b) \quad (2.14)$$

$${}^t c_{eq} = c_{eq}^{des} \quad (RH < RH_b) \quad (2.15)$$

If the change of direction is reversed, from desorption to adsorption (${}^{t-\Delta t}\kappa = -1$, ${}^t\kappa = 1$), the following conditions yield for the interior sorption path.

$$\begin{aligned} \left. \frac{dc_{eq}^{int}}{dRH} \right|_{RH=t-\Delta t RH} &= K_a \left. \frac{d{}^{t-\Delta t}c_{eq}}{dRH} \right|_{RH=t-\Delta t RH} \\ \left. \frac{dc_{eq}^{int}}{dRH} \right|_{RH=RH_b} &= \left. \frac{dc_{eq}^{ads}}{dRH} \right|_{RH=RH_b} \quad RH_b > {}^{t-\Delta t} RH \\ c_{eq}^{int}({}^{t-\Delta t} RH) &= {}^{t-\Delta t}c_{eq}({}^{t-\Delta t} RH) \\ c_{eq}^{int}(RH_b) &= c_{eq}^{ads}(RH_b) \end{aligned}$$

where RH_b is the junction point of interior sorption path and boundary adsorption curve. The new sorption path is described by

$${}^t c_{eq} = c_{eq}^{int} \quad (RH < RH_b) \quad (2.16)$$

$${}^t c_{eq} = c_{eq}^{ads} \quad (RH > RH_b) \quad (2.17)$$

The solution of the parameters RH_b , α^{int} , β^{int} , γ^{int} , governing c_{eq}^{int} is referred to Nyman [4].

Having established c_{eq} as a function of relative humidity, it is necessary to define c_{eq} in terms of vapor density in conjunction with the transport model. Therefore the temperature must be taken into account as it governs the level of relative humidity. However, thermodynamic effects such as latent heat of condensation are neglected.

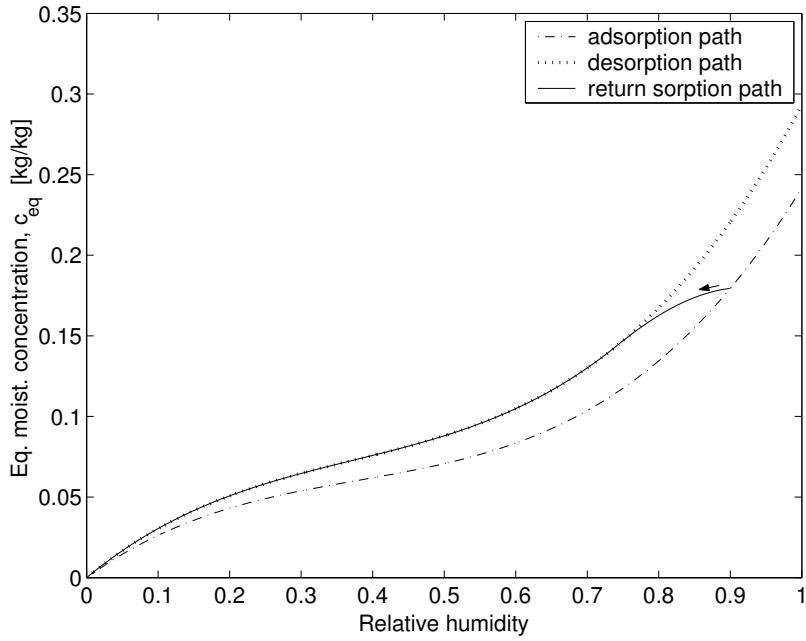


Figure 2.2: Return sorption path with interior hysteresis of 2:nd order, $K_d = 0.1$

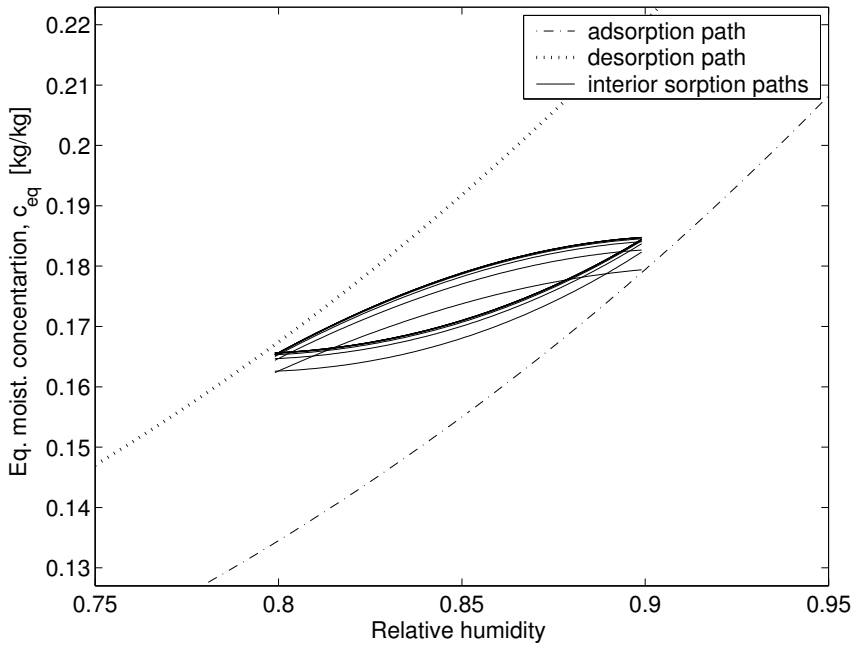


Figure 2.3: Cycled hysteresis curves, $K_a = K_d = 0.1$

Chapter 3

Experimental study of sorption in paper

3.1 Method

An experimental study is performed in order to measure sorption characteristics of the material used in the simulations and the object is to obtain the boundary sorption equilibrium curves during adsorption and desorption, respectively. The experimental guidelines in [7] are followed and the study is carried out using 6 samples of the liner material Whitetop 200 [g/m²], 200WT.

The samples are dried in an oven, weighed and placed in a climate chamber where the relative humidity RH is controlled with an accuracy of ± 1 % using the gauge instrument Visala X3910020. The equilibrium moisture concentration, c_{eq} [kg/kg], is evaluated at increasing levels of RH from 19 %, 30 %, 40 %, 49 %, 59 %, 69 %, 77 % and up to 92 %. These are mean values and RH is fluctuating ± 2 % about 5-8 times per hour except for the level at 92 %, where the the fluctuation is ± 4 % every hour. The temperature is kept constant at 23 ± 2 °C.

When the samples reach equilibrium with 92 % 4 samples are soaked with water. The last 2 samples are kept at 92 % in order to obtain an interior desorption curve. The equilibrium moisture concentration is then evaluated at decreasing levels of RH from 92 % down to 19 %.

3.2 Result

The adsorption and the desorption curves are fitted by least squares to third order polynomials according to (3.1) and (3.2), see also figure 3.1. The interior desorption of second order is shown in figure 3.2. The measured values of c_{eq} can be found in Appendix A.

$$c_{eq}^{ads}(RH) = 0.3204 RH - 0.6374 RH^2 + 0.5588 RH^3 \quad (3.1)$$

$$c_{eq}^{des}(RH) = 0.3674 RH - 0.6914 RH^2 + 0.6172 RH^3 \quad (3.2)$$

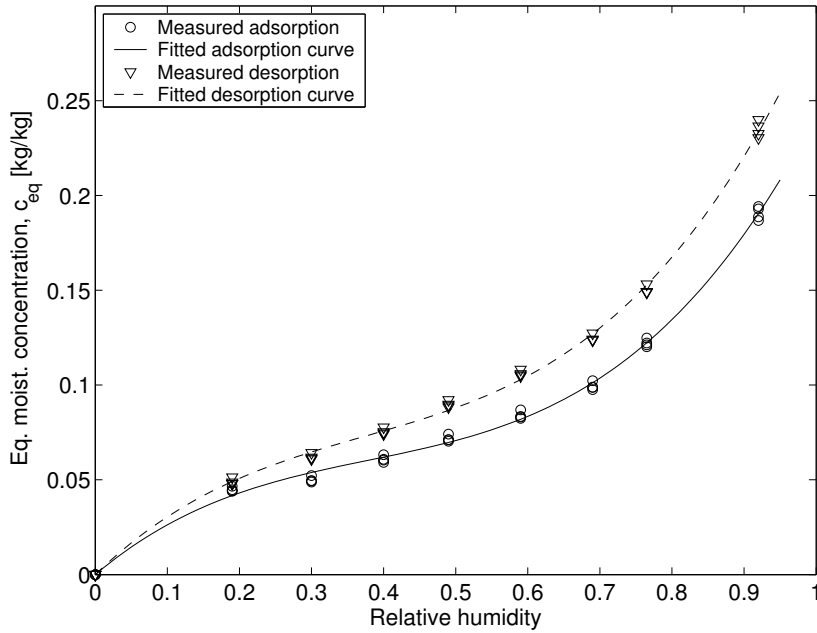


Figure 3.1: 200WT, fitted adsorption and desorption curves

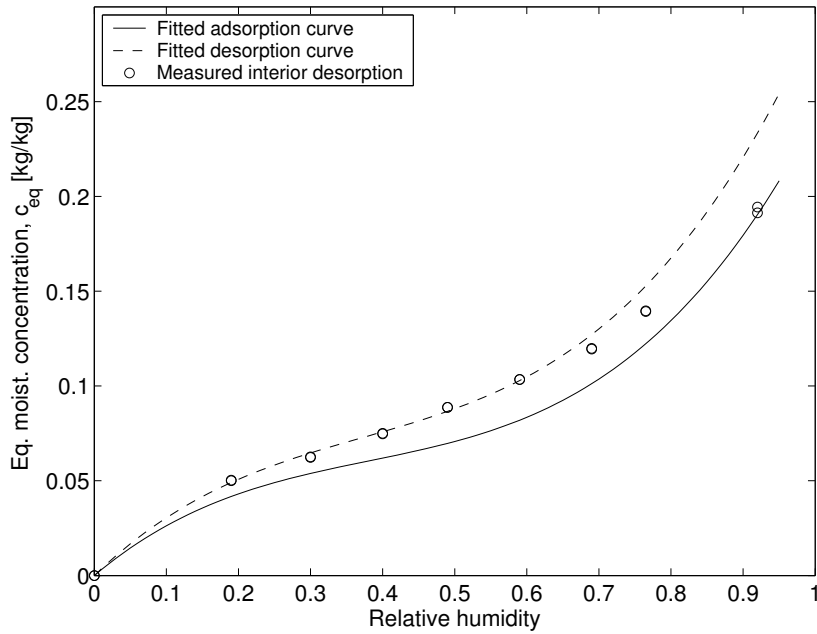


Figure 3.2: 200WT, measured interior desorption and fitted adsorption and desorption curves

Chapter 4

Numerical formulation

The object of the numerical formulation is to derive element equations for the transport model in the two-dimensional case and to describe the computing implementation.

4.1 Derivation of element equations

4.1.1 Strong form

The differential equations derived in section 2.1 describing the transport model, including boundary and initial value conditions, constitute the strong form of the boundary-initial value problem, BIVP.

$$\varepsilon \dot{\rho}_v + \rho_s \dot{c}_l - \nabla^T \cdot (D_v \mathbf{I} \nabla \rho_v) = 0 \quad \text{in the region } \Omega \quad (4.1)$$

$$\dot{c}_l - k_c (c_{eq}(\rho_v) - c_l) = 0 \quad \text{in the region } \Omega \quad (4.2)$$

$$(D_v \mathbf{I} \nabla \rho_v)^T \cdot \mathbf{n} = k_b (\rho_{v,\infty} - \rho_{v,\partial\Omega_c}) \quad \text{at boundary } \partial\Omega_c \quad (4.3)$$

$$(D_v \mathbf{I} \nabla \rho_v)^T \cdot \mathbf{n} = 0 \quad \text{at boundary } \partial\Omega_s \quad (4.4)$$

$$\rho_v(t = 0) = \rho_0 \quad \text{in the region } \Omega \quad (4.5)$$

$$c_l(t = 0) = c_{eq}(\rho_0) \quad \text{in the region } \Omega \quad (4.6)$$

where $\partial\Omega_c$ denotes the convective boundary and $\partial\Omega_s$ the boundary where the flux is zero for instance due to symmetry.

4.1.2 Weak form

Having established the system of differential equations in the BIVP we shall now introduce the weak form.

We first look at the diffusion equation (4.1). Multiplying with an arbitrary weight function that we may choose as $\delta\rho_v$ and integrating over the region Ω gives

$$\delta\rho_v \int_{\Omega} [\varepsilon\dot{\rho}_v + \rho_s\dot{c}_l - \nabla^T \cdot (D_v\mathbf{I}\nabla\rho_v)] dV = \delta F_a \quad (4.7)$$

where δF_a expresses the offset of the equilibrium. In case of equilibrium $\delta F_a = 0$

Developing (4.7) using the product rule and then the Gauss theorem followed by insertion of \dot{c}_l and the boundary condition result in the following expression

$$\begin{aligned} & \delta\rho_v \int_{\Omega} [\varepsilon\dot{\rho}_v + \rho_s\dot{c}_l - \nabla^T \cdot (D_v\mathbf{I}\nabla\rho_v)] dV = \\ & \varepsilon \int_{\Omega} \delta\rho_v\dot{\rho}_v dV + \rho_s \int_{\Omega} \delta\rho_v\dot{c}_l dV - \int_{\Omega} \delta\rho_v\nabla^T \cdot (D_v\mathbf{I}\nabla\rho_v) dV = \\ & \varepsilon \int_{\Omega} \delta\rho_v\dot{\rho}_v dV + \rho_s \int_{\Omega} \delta\rho_v\dot{c}_l dV - \int_{\Omega} \nabla^T \cdot (\delta\rho_v D_v\mathbf{I}\nabla\rho_v) dV + \\ & \qquad \qquad \qquad \int_{\Omega} \nabla\delta\rho_v \cdot (D_v\mathbf{I}\nabla\rho_v) dV = \\ & \varepsilon \int_{\Omega} \delta\rho_v\dot{\rho}_v dV + \rho_s \int_{\Omega} \delta\rho_v\dot{c}_l dV - \oint_{\partial\Omega} (\delta\rho_v D_v\mathbf{I}\nabla\rho_v)^T \cdot \mathbf{n} dS + \\ & \qquad \qquad \qquad \int_{\Omega} \nabla\delta\rho_v \cdot (D_v\mathbf{I}\nabla\rho_v) dV = \\ & \varepsilon \int_{\Omega} \delta\rho_v\dot{\rho}_v dV + \rho_s k_c \int_{\Omega} \delta\rho_v c_{eq}(\rho_v) dV - \rho_s k_c \int_{\Omega} \delta\rho_v c_l dV + \\ & \qquad k_b \oint_{\partial\Omega_c} \delta\rho_v(\rho_{v,\partial\Omega_c} - \rho_{v,\infty}) dS + \int_{\Omega} \nabla\delta\rho_v \cdot (D_v\mathbf{I}\nabla\rho_v) dV = \delta F_a \quad (4.8) \end{aligned}$$

Looking at equation (4.2) we introduce the weight function δc_l and integrate over Ω . This leads to the following expression for the offset δF_b of equilibrium governing the mass transfer phenomena in the interface between the void and fibre space.

$$\begin{aligned} & \delta c_l \int_{\Omega} [\dot{c}_l - k_c(c_{eq}(\rho_v) - c_l)] dV = \\ & \int_{\Omega} \delta c_l\dot{c}_l dV - k_c \int_{\Omega} \delta c_l c_{eq}(\rho_v) dV + k_c \int_{\Omega} \delta c_l c_l dV = \delta F_b \quad (4.9) \end{aligned}$$

In order to reach equilibrium we wish to find an expression in terms of increments $\Delta\rho_v$, Δc_l that stepwise approaches the correct solution of ρ_v and c_l . By linearizing explicitly with 1:st order partial derivatives of ρ_v and c_l the following equations are obtained.

$$\frac{\partial}{\partial\rho_v} \delta F_a \Delta\rho_v + \frac{\partial}{\partial c_l} \delta F_a \Delta c_l = -\delta F_a \quad (4.10)$$

$$\frac{\partial}{\partial\rho_v} \delta F_b \Delta\rho_v + \frac{\partial}{\partial c_l} \delta F_b \Delta c_l = -\delta F_b \quad (4.11)$$

By evaluating the left-hand side of (4.10) the following incremental terms will emerge

$$\begin{aligned}
\frac{\partial}{\partial \rho_v} \varepsilon \int_{\Omega} \delta \rho_v \dot{\rho}_v dV \Delta \rho_v &= \varepsilon \int_{\Omega} \delta \rho_v \Delta \dot{\rho}_v dV \\
\frac{\partial}{\partial \rho_v} \rho_s k_c \int_{\Omega} \delta \rho_v c_{eq}(\rho_v) dV \Delta \rho_v &= \rho_s k_c \int_{\Omega} \delta \rho_v \frac{\partial c_{eq}}{\partial \rho_v} \Delta \rho_v dV \\
-\frac{\partial}{\partial c_l} \rho_s k_c \int_{\Omega} \delta \rho_v c_l dV \Delta c_l &= -\rho_s k_c \int_{\Omega} \delta \rho_v \Delta c_l dV \\
\frac{\partial}{\partial \rho_v} k_b \oint_{\partial \Omega_c} \delta \rho_v (\rho_{v,\infty} - \rho_{v,\partial \Omega_c}) dS \Delta \rho_v &= k_b \oint_{\partial \Omega_c} \delta \rho_v \Delta \rho_{v,\partial \Omega_c} dS \\
\frac{\partial}{\partial \rho_v} \int_{\Omega} \nabla \delta \rho_v \cdot (D_v \mathbf{I} \nabla \rho_v) dV \Delta \rho_v &= \int_{\Omega} \nabla \delta \rho_v \cdot D_v \mathbf{I} \nabla (\Delta \rho_v) dV \quad (4.12)
\end{aligned}$$

and from (4.11)

$$\begin{aligned}
\frac{\partial}{\partial c_l} \int_{\Omega} \delta c_l \dot{c}_l dV \Delta c_l &= \int_{\Omega} \delta c_l \Delta \dot{c}_l dV \\
-\frac{\partial}{\partial \rho_v} k_c \int_{\Omega} \delta c_l c_{eq}(\rho_v) dV \Delta \rho_v &= -k_c \int_{\Omega} \delta c_l \frac{c_{eq}}{\rho_v} \Delta \rho_v dV \\
\frac{\partial}{\partial c_l} k_c \int_{\Omega} \delta c_l c_l dV \Delta c_l &= k_c \int_{\Omega} \delta c_l \Delta c_l dV \quad (4.13)
\end{aligned}$$

Inserting δF_a and δF_b from (4.8) and (4.9) and the incremental terms obtained in (4.12) and (4.13) into (4.10) and (4.11) the linearized weak form can be formed.

$$\begin{aligned}
&\varepsilon \int_{\Omega} \delta \rho_v \Delta \dot{\rho}_v dV + \rho_s k_c \int_{\Omega} \delta \rho_v \frac{\partial c_{eq}}{\partial \rho_v} \Delta \rho_v dV - \rho_s k_c \int_{\Omega} \delta \rho_v \Delta c_l dV + \\
&\quad k_b \oint_{\partial \Omega_c} \delta \rho_v \Delta \rho_{v,\partial \Omega_c} dS + \int_{\Omega} \nabla \delta \rho_v \cdot D_v \mathbf{I} \nabla (\Delta \rho_v) dV = \\
&-\varepsilon \int_{\Omega} \delta \rho_v \dot{\rho}_v dV - \rho_s k_c \int_{\Omega} \delta \rho_v c_{eq}(\rho_v) dV + \rho_s k_c \int_{\Omega} \delta \rho_v c_l dV - \\
&\quad k_b \oint_{\partial \Omega_c} \delta \rho_v (\rho_{v,\partial \Omega_c} - \rho_{v,\infty}) dS - \int_{\Omega} \nabla \delta \rho_v \cdot (D_v \mathbf{I} \nabla \rho_v) dV \quad (4.14)
\end{aligned}$$

$$\begin{aligned}
&\int_{\Omega} \delta c_l \Delta \dot{c}_l dV - k_c \int_{\Omega} \delta c_l \frac{c_{eq}}{\rho_v} \Delta \rho_v dV + k_c \int_{\Omega} \delta c_l \Delta c_l dV = \\
&-\int_{\Omega} \delta c_l \dot{c}_l dV + k_c \int_{\Omega} \delta c_l c_{eq}(\rho_v) dV - k_c \int_{\Omega} \delta c_l c_l dV \quad (4.15)
\end{aligned}$$

4.1.3 Finite element formulation

A 2-dimensional 4-node isoparametric element with 8 degrees of freedom is introduced.

The vapor density ρ_v and moisture concentration c_l are approximated as follows

$$\begin{aligned}\rho_v(x, y) &= \mathbf{N}_a^e \mathbf{a}^e \\ c_l(x, y) &= \mathbf{N}_b^e \mathbf{a}^e\end{aligned}\tag{4.16}$$

where

$$\mathbf{N}_a^e = [N_1^e \quad 0 \quad N_2^e \quad 0 \quad N_3^e \quad 0 \quad N_4^e \quad 0]$$

$$\mathbf{N}_b^e = [0 \quad N_1^e \quad 0 \quad N_2^e \quad 0 \quad N_3^e \quad 0 \quad N_4^e]$$

are the element shape functions in the global coordinate system (x,y) and

$$\mathbf{a}^e = [\rho_{v,1} \quad c_{l,1} \quad \rho_{v,2} \quad c_{l,2} \quad \rho_{v,3} \quad c_{l,3} \quad \rho_{v,4} \quad c_{l,4}]^T$$

are the nodal values of ρ_v and c_l . The same relations as in (4.16) holds for the incremental form of vapor density and moisture concentration.

The \mathbf{B}_a^e -matrix is given by

$$\mathbf{B}_a^e = \nabla \mathbf{N}_a^e$$

where

$$\nabla = \begin{bmatrix} \frac{\partial}{\partial x} \\ \frac{\partial}{\partial y} \end{bmatrix}$$

4.1.4 Paper element

The incremental terms in the left-hand side of (4.14) and (4.15) are approximated in the 2-dimensional case, by integrating over the element area A and multiplying with the thickness h . The following terms provide contribution to the conductivity matrix \mathbf{C}^e and the stiffness matrix \mathbf{K}^e .

$$h\varepsilon \int_A \delta\rho_v \Delta\rho_v dA = \delta\mathbf{a}^{eT} \mathbf{C}_{a\rho}^e \Delta\mathbf{a}^e \quad \Rightarrow \quad \mathbf{C}_{a\rho}^e = h\varepsilon \int_A \mathbf{N}_a^{eT} \mathbf{N}_a^e dA \quad (4.17)$$

$$h\rho_s k_c \int_A \delta\rho_v \frac{\partial c_{eq}}{\partial \rho_v} \Delta\rho_v dA = \delta\mathbf{a}^{eT} \mathbf{K}_{ai}^e \Delta\mathbf{a}^e \quad \Rightarrow \quad \mathbf{K}_{ai}^e = h\rho_s k_c \int_A \mathbf{N}_a^{eT} \frac{\partial c_{eq}}{\partial \rho_v} \mathbf{N}_a^e dA \quad (4.18)$$

$$-h\rho_s k_c \int_A \delta\rho_v \Delta c_l dA = \delta\mathbf{a}^{eT} \mathbf{K}_{ac}^e \Delta\mathbf{a}^e \quad \Rightarrow \quad \mathbf{K}_{ac}^e = -h\rho_s k_c \int_A \mathbf{N}_a^{eT} \mathbf{N}_b^e dA \quad (4.19)$$

$$hk_b \oint_{\partial A_c} \delta\rho_v \Delta\rho_{v,\partial\Omega_c} dL = \delta\mathbf{a}^{eT} \mathbf{K}_{\partial A_c}^e \Delta\mathbf{a}^e \quad \Rightarrow \quad \mathbf{K}_{\partial A_c}^e = hk_b \oint_{\partial A_c} \mathbf{N}_a^{eT} \mathbf{N}_a^e dL \quad (4.20)$$

$$h \int_A \nabla \delta\rho_v \cdot D_v \mathbf{I} \nabla (\Delta\rho_v) dA = \delta\mathbf{a}^{eT} \mathbf{K}_{av}^e \Delta\mathbf{a}^e \quad \Rightarrow \quad \mathbf{K}_{av}^e = h \int_A \mathbf{B}_a^{eT} D_v \mathbf{I} \mathbf{B}_a^e dA \quad (4.21)$$

$$h \int_A \delta c_l \Delta c_l dA = \delta\mathbf{a}^{eT} \mathbf{C}_{bc}^e \Delta\mathbf{a}^e \quad \Rightarrow \quad \mathbf{C}_{bc}^e = h \int_A \mathbf{N}_b^{eT} \mathbf{N}_b^e dA \quad (4.22)$$

$$-hk_c \int_A \delta c_l \frac{c_{eq}}{\rho_v} \Delta\rho_v dA = \delta\mathbf{a}^{eT} \mathbf{K}_{bi}^e \Delta\mathbf{a}^e \quad \Rightarrow \quad \mathbf{K}_{bi}^e = -hk_c \int_A \mathbf{N}_b^{eT} \frac{\partial c_{eq}}{\partial \rho_v} \mathbf{N}_a^e dA \quad (4.23)$$

$$hk_c \int_A \delta c_l \Delta c_l dA = \delta\mathbf{a}^{eT} \mathbf{K}_{bc}^e \Delta\mathbf{a}^e \quad \Rightarrow \quad \mathbf{K}_{bc}^e = hk_c \int_A \mathbf{N}_b^{eT} \mathbf{N}_b^e dA \quad (4.24)$$

The known quantities in the right-hand side of (4.14) and (4.15) are now approximated in the same manner. The terms emerging from this integration all provide contribution to the residual vector \mathbf{Q}^e . They are all functions of the nodal values and are to be updated in each iteration step except for the term \mathbf{Q}_{ext}^e governed by $\rho_{v,\infty}$ which is an external fixed quantity defined for each time step.

$$-h\varepsilon \int_A \delta \rho_v \dot{\rho}_v dA = \delta \mathbf{a}^{eT} \dot{\mathbf{Q}}_{a\rho}^e \quad \Rightarrow \quad \dot{\mathbf{Q}}_{a\rho}^e = -\mathbf{C}_{a\rho}^e \dot{\mathbf{a}}^e \quad (4.25)$$

$$-h\rho_s k_c \int_A \delta \rho_v c_{eq}(\rho_v) dA = \delta \mathbf{a}^{eT} \mathbf{Q}_{ai}^e \quad \Rightarrow \quad \mathbf{Q}_{ai}^e = -h\rho_s k_c \int_A \mathbf{N}_a^{eT} c_{eq} dA \quad (4.26)$$

$$h\rho_s k_c \int_A \delta \rho_v c_l dA = \delta \mathbf{a}^{eT} \mathbf{Q}_{ac}^e \quad \Rightarrow \quad \mathbf{Q}_{ac}^e = -\mathbf{K}_{ac}^e \mathbf{a}^e \quad (4.27)$$

$$-hk_b \oint_{\partial A_c} \delta \rho_v (\rho_{v,\partial\Omega_c} - \rho_{v,\infty}) dL = \delta \mathbf{a}^{eT} (\mathbf{Q}_{\partial A_c}^e - \mathbf{Q}_{ext}^e) \quad (4.28)$$

$$\Rightarrow \quad \mathbf{Q}_{\partial A_c}^e = -\mathbf{K}_{\partial A_c}^e \mathbf{a}^e \quad (4.28)$$

$$\Rightarrow \quad \mathbf{Q}_{ext}^e = -\mathbf{K}_{\partial A_c}^e \mathbf{a}_\infty \quad (4.29)$$

$$-h \int_A \nabla \delta \rho_v \cdot (D_v \mathbf{I} \nabla \rho_v) dA = \delta \mathbf{a}^{eT} \mathbf{Q}_{av}^e \quad \Rightarrow \quad \mathbf{Q}_{av}^e = -\mathbf{K}_{av}^e \mathbf{a}^e \quad (4.30)$$

$$-h \int_A \delta c_l \dot{c}_l dA = \delta \mathbf{a}^{eT} \dot{\mathbf{Q}}_{bc}^e \quad \Rightarrow \quad \dot{\mathbf{Q}}_{bc}^e = -\mathbf{C}_{bc}^e \dot{\mathbf{a}}^e \quad (4.31)$$

$$hk_c \int_A \delta c_l c_{eq}(\rho_v) dA = \delta \mathbf{a}^{eT} \mathbf{Q}_{bi}^e \quad \Rightarrow \quad \mathbf{Q}_{bi}^e = hk_c \int_A \mathbf{N}_b^{eT} c_{eq} dA \quad (4.32)$$

$$-hk_c \int_A \delta c_l c_l dA = \delta \mathbf{a}^{eT} \mathbf{Q}_{bc}^e \quad \Rightarrow \quad \mathbf{Q}_{bc}^e = -\mathbf{K}_{bc}^e \mathbf{a}^e \quad (4.33)$$

The conductivity matrix, the stiffness matrix and the residual vector can then be put together as follows.

$$\mathbf{C}^e = \mathbf{C}_{ap}^e + \mathbf{C}_{bc}^e$$

$$\mathbf{K}^e = \mathbf{K}_{ai}^e + \mathbf{K}_{ac}^e + \mathbf{K}_{\partial A_c}^e + \mathbf{K}_{av}^e + \mathbf{K}_{bi}^e + \mathbf{K}_{bc}^e$$

$$\mathbf{Q}^e = \dot{\mathbf{Q}}_{av}^e + \mathbf{Q}_{ai}^e + \mathbf{Q}_{ac}^e + \mathbf{Q}_{\partial A_c}^e + \mathbf{Q}_{av}^e + \dot{\mathbf{Q}}_{bc}^e + \mathbf{Q}_{bi}^e + \mathbf{Q}_{bc}^e - \mathbf{Q}_{ext}^e$$

and the paper element equation is established

$$\left(\frac{1}{\Delta t} \mathbf{C}^e + \mathbf{K}^e\right) \Delta \mathbf{a}^e = \mathbf{Q}^e \quad (4.34)$$

○ nodal points

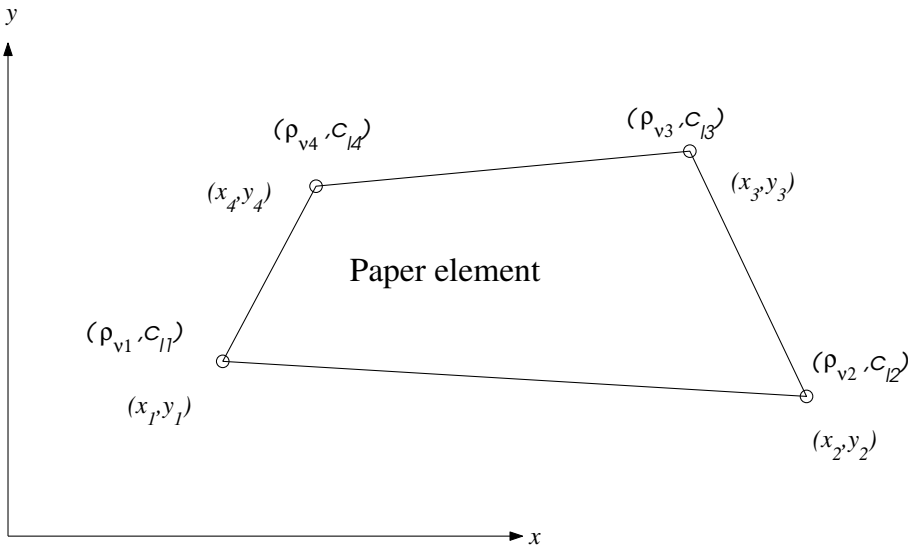


Figure 4.1: 4-node isoparametric paper element

4.1.5 Air element

In the air cells between the paper sheets and inside the box the moisture transport occurs by vapor diffusion and possible convection. Here the air is assumed to be still and only transport by diffusion is considered. The degrees of freedom governed by the moisture concentration c_i are excluded since liquid water in the air is not considered.

This reduces the BIVP to

$$\dot{\rho}_v - \nabla^T \cdot (D_v \mathbf{I} \nabla \rho_v) = 0 \quad \text{in the region } \Omega \quad (4.35)$$

$$D_v \mathbf{I} \nabla \rho_v|_{\partial\Omega} = 0 \quad \text{at boundary } \partial\Omega_s \quad (4.36)$$

$$\rho_v(t=0) = \rho_0 \quad \text{in the region } \Omega \quad (4.37)$$

An expression for the equilibrium offset δF of diffusion equation (4.35) is obtained after multiplying with the weight function $\delta\rho_v$ and integrating.

$$\begin{aligned} \delta\rho_v \int_{\Omega} [\dot{\rho}_v - \nabla^T \cdot (D_v \mathbf{I} \nabla \rho_v)] dV &= \\ \int_{\Omega} \delta\rho_v \dot{\rho}_v dV - \int_{\Omega} \delta\rho_v \nabla^T \cdot (D_v \mathbf{I} \nabla \rho_v) dV &= \\ \int_{\Omega} \delta\rho_v \dot{\rho}_v dV - \int_{\Omega} \nabla^T \cdot (\delta\rho_v D_v \mathbf{I} \nabla \rho_v) dV + \int_{\Omega} \nabla \delta\rho_v \cdot (D_v \mathbf{I} \nabla \rho_v) dV &= \\ \int_{\Omega} \delta\rho_v \dot{\rho}_v dV - \oint_{\partial\Omega} (\delta\rho_v D_v \mathbf{I} \nabla \rho_v)^T \cdot \mathbf{n} dS + \int_{\Omega} \nabla \delta\rho_v \cdot (D_v \mathbf{I} \nabla \rho_v) dV &= \\ \int_{\Omega} \delta\rho_v \dot{\rho}_v dV + \int_{\Omega} \nabla \delta\rho_v \cdot (D_v \mathbf{I} \nabla \rho_v) dV &= \delta F \end{aligned} \quad (4.38)$$

By linearizing the weak form is obtained.

$$\begin{aligned} \frac{\partial}{\partial \rho_v} \delta F \Delta \rho_v &= -\delta F \\ &\Leftrightarrow \\ \int_{\Omega} \delta\rho_v \Delta \dot{\rho}_v dV + \int_{\Omega} \nabla \delta\rho_v \cdot D_v \mathbf{I} \nabla (\Delta \rho_v) dV &= - \int_{\Omega} \delta\rho_v \dot{\rho}_v dV \\ &\quad - \int_{\Omega} \nabla \delta\rho_v \cdot (D_v \mathbf{I} \nabla \rho_v) dV \end{aligned} \quad (4.39)$$

With use of previously defined approximating functions the terms in the weak form provide the following contribution to the air element equation

$$h \int_A \delta\rho_v \Delta \dot{\rho}_v dA = \delta \mathbf{a}^{eT} \mathbf{C}_{a\rho}^e \Delta \dot{\mathbf{a}}^e \quad \Rightarrow \quad \mathbf{C}_{a\rho}^e = h \int_A \mathbf{N}_a^{eT} \mathbf{N}_a^e dA \quad (4.40)$$

$$h \int_A \nabla \delta\rho_v \cdot D_v \mathbf{I} \nabla (\Delta \rho_v) dA = \delta \mathbf{a}^{eT} \mathbf{K}_{av}^e \Delta \mathbf{a}^e \quad \Rightarrow \quad \mathbf{K}_{av}^e = h \int_A \mathbf{B}_a^{eT} D_v \mathbf{I} \mathbf{B}_a^e dA \quad (4.41)$$

$$-h \int_A \delta\rho_v \dot{\rho}_v dA = \delta \mathbf{a}^{eT} \dot{\mathbf{Q}}_{a\rho}^e \quad \Rightarrow \quad \dot{\mathbf{Q}}_{a\rho}^e = -\mathbf{C}_{a\rho}^e \dot{\mathbf{a}}^e \quad (4.42)$$

$$-h \int_A \nabla \delta\rho_v \cdot (D_v \mathbf{I} \nabla \rho_v) dA = \delta \mathbf{a}^{eT} \mathbf{Q}_{av}^e \quad \Rightarrow \quad \mathbf{Q}_{av}^e = -\mathbf{K}_{av}^e \mathbf{a}^e \quad (4.43)$$

With following definitions

$$\begin{aligned} \mathbf{C}^e &= \mathbf{C}_{a\rho}^e \\ \mathbf{K}^e &= \mathbf{K}_{av}^e \\ \mathbf{Q}^e &= \dot{\mathbf{Q}}_{a\rho}^e + \mathbf{Q}_{av}^e \end{aligned}$$

the air element equation is established.

$$\left(\frac{1}{\Delta t} \cdot \mathbf{C}^e + \mathbf{K}^e\right) \Delta \mathbf{a}^e = \mathbf{Q}^e \quad (4.44)$$

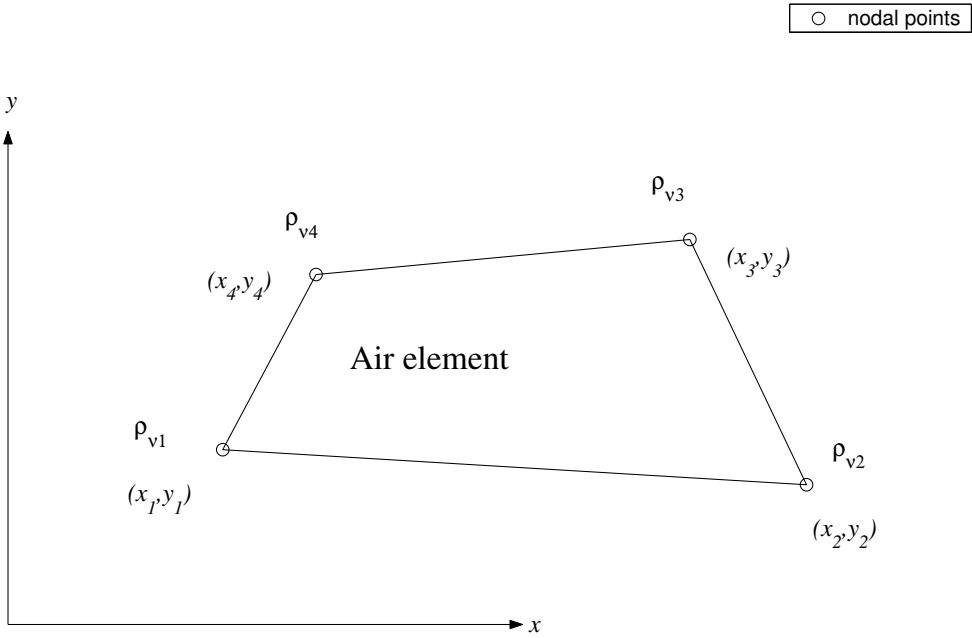


Figure 4.2: 4-node isoparametric air element

4.1.6 Gauss integration

Evaluation of the integrals is done using gauss integration (2×2) in the local coordinate system (ξ, η) . The shape functions in the (ξ, η) system are given by

$$\begin{aligned} \bar{N}_1^e &= \frac{1}{4}(1 - \xi)(1 - \eta) & \bar{N}_2^e &= \frac{1}{4}(1 + \xi)(1 - \eta) \\ \bar{N}_3^e &= \frac{1}{4}(1 + \xi)(1 + \eta) & \bar{N}_4^e &= \frac{1}{4}(1 - \xi)(1 + \eta) \end{aligned}$$

and the shape function vectors used in the integration are

$$\begin{aligned}\bar{\mathbf{N}}_a^e &= [\bar{N}_1^e \ 0 \ \bar{N}_2^e \ 0 \ \bar{N}_3^e \ 0 \ \bar{N}_4^e \ 0] \\ \bar{\mathbf{N}}_b^e &= [0 \ \bar{N}_1^e \ 0 \ \bar{N}_2^e \ 0 \ \bar{N}_3^e \ 0 \ \bar{N}_4^e]\end{aligned}$$

The $\bar{\mathbf{B}}_a^e$ -matrix is given by

$$\bar{\mathbf{B}}_a^e = \nabla \bar{\mathbf{N}}_a^e = \begin{bmatrix} \frac{\partial}{\partial x} \\ \frac{\partial}{\partial y} \end{bmatrix} \bar{\mathbf{N}}_a^e = (\mathbf{J}^T)^{-1} \begin{bmatrix} \frac{\partial}{\partial \xi} \\ \frac{\partial}{\partial \eta} \end{bmatrix} \bar{\mathbf{N}}_a^e$$

where \mathbf{J} is the Jacobian matrix

$$\mathbf{J} = \begin{bmatrix} \frac{\partial x}{\partial \xi} & \frac{\partial x}{\partial \eta} \\ \frac{\partial y}{\partial \xi} & \frac{\partial y}{\partial \eta} \end{bmatrix}$$

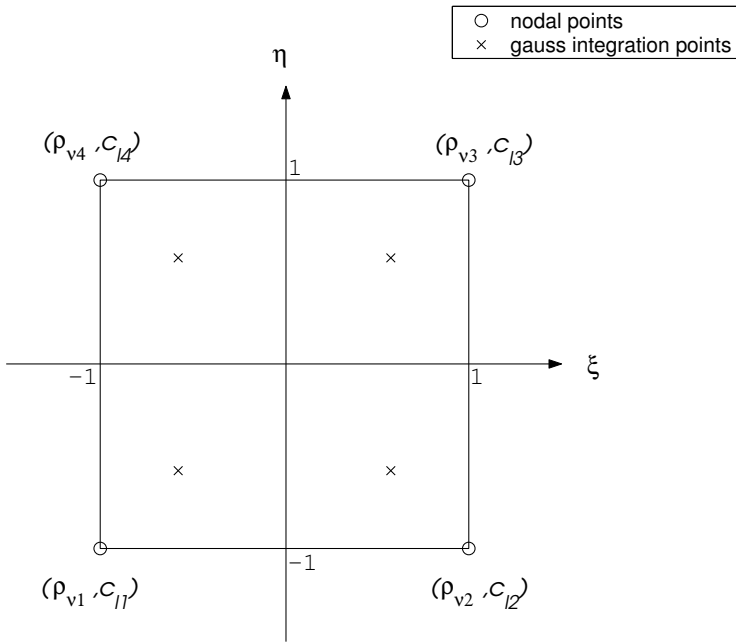


Figure 4.3: Local element coordinate system for (2×2) gauss integration

4.2 Computing implementation

The strategy in order to calculate the nodal values as a function of time is to define a discrete time history in accordance to

$$t = \Delta t \cdot n \quad n = \{1, 2, \dots\} \quad (4.45)$$

and then perform time integration at each time step using a combined Newton-Raphson and Euler backward method.

4.2.1 Time integration

Given the nodal values ${}^{t-\Delta t}\mathbf{a}$ at a known instant of time $t - \Delta t$ an iterative procedure is used to integrate nodal values ${}^t\mathbf{a}$ at instant of time t . At each iteration an increment $\Delta\mathbf{a}_{i-1}$ of the nodal value is implicitly calculated from the assembled equation system (4.46).

$$\left(\frac{1}{\Delta t} \cdot \mathbf{C} + \mathbf{K}\right)_{i-1} \Delta\mathbf{a}_{i-1} = \mathbf{Q}_{i-1} \quad (4.46)$$

where the matrix $\left(\frac{1}{\Delta t} \cdot \mathbf{C} + \mathbf{K}\right)_{i-1}$ is updated and inverted at each iteration in accordance with the full Newton-Raphson method. The residual vector \mathbf{Q}_{i-1} describes the offset of the numerical equilibrium at time point t in accordance to Euler backward method.

The temperature tT and vapor density outside the box ${}^t\mathbf{a}_\infty$ are external input variables and valid at time point t . Also the temperature at the previous time step ${}^{t-\Delta t}T$ must be taken into account while updating the sorption path.

This updating procedure at iteration i is expressed in the following order.

- \mathbf{a}_{i-1} *given from previous iteration*
- $\dot{\mathbf{a}}_{i-1} = \frac{\mathbf{a}_{i-1} - {}^t\mathbf{a}}{\Delta t}$
- $\mathbf{a}_{i-1}, {}^{t-\Delta t}T, {}^tT \Rightarrow (c_{eq}(\rho_v), \frac{\partial c_{eq}}{\partial \rho_v})_{i-1}$
- $(\frac{\partial c_{eq}}{\partial \rho_v})_{i-1} \Rightarrow (\frac{1}{\Delta t} \cdot \mathbf{C} + \mathbf{K})_{i-1}$
- $(c_{eq}(\rho_v))_{i-1}, \mathbf{a}_{i-1}, \dot{\mathbf{a}}_{i-1}, {}^t\mathbf{a}_\infty \Rightarrow \mathbf{Q}_{i-1}$
- $(\frac{1}{\Delta t} \cdot \mathbf{C} + \mathbf{K})_{i-1} \cdot {}^t\Delta\mathbf{a}_{i-1} = \mathbf{Q}_{i-1} \Rightarrow \Delta\mathbf{a}_{i-1}$
- $\mathbf{a}_i = \mathbf{a}_{i-1} + \Delta\mathbf{a}_{i-1}$

4.2.2 Schematic program

The different steps of the actual computing procedure in the main program are summarized as:

- definition of constant parameters $D_v, k_b, k_c, \varepsilon, \rho_p$
- definition of element shape properties and topology $Ex, Ey, Edof$
- definition of input parameters ${}^tT, {}^t\mathbf{a}_\infty$
- calculation of constant parts of conductivity and stiffness matrices

$$\mathbf{C}_{const}^e, \mathbf{K}_{const}^e \quad \text{see table 4.1}$$

- initiation of nodal start values ${}^{t=0}\mathbf{a}, \mathbf{a}_{i=0}$
- initiation of sorption quantities

$$c_{eq}^{ads}(RH), c_{eq}^{des}(RH) \quad , \quad K_a, K_d, [c_{eq}(RH), RH_b, \kappa]_{i=0}$$

$$\left[c_{eq}(\rho_v), \frac{\partial c_{eq}}{\partial \rho_v} \right]_{i=0} = f([c_{eq}(RH), \mathbf{a}]_{i=0}, {}^{t=t_1}T)$$

for $n = \{1, 2, \dots\} \quad t = \Delta t \cdot n$

iterating $i = \{1, 2, \dots\} \quad \text{until} \quad \text{norm}(\mathbf{Q}_{i-1}) < \epsilon$

- calculation of non-linear parts of stiffness matrices and residual vectors

$$\mathbf{K}^e \left(\frac{\partial c_{eq}}{\partial \rho_v} \Big|_{i-1} \right), \mathbf{Q}^e(c_{eq}(\rho_v)_{i-1}), \mathbf{Q}^e(\mathbf{a}_{i-1}) \quad \text{see table 4.2}$$

- assemblage of global conductivity/stiffness matrix and residual vector

$$\left(\frac{1}{\Delta t} \cdot \mathbf{C} + \mathbf{K} \right)_{i-1}, \mathbf{Q}_{i-1}$$

- solving the equation and updating nodal values

$$\left(\frac{1}{\Delta t} \cdot \mathbf{C} + \mathbf{K} \right)_{i-1} \cdot \Delta \mathbf{a}_{i-1} = \mathbf{Q}_{i-1}, \quad \mathbf{a}_i = \mathbf{a}_{i-1} + \Delta \mathbf{a}_{i-1}$$

- updating sorption quantities $[c_{eq}(RH), RH_b, \kappa]_i =$

$$f({}^{t-\Delta t}\mathbf{a}, \mathbf{a}_i, c_{eq}^{ads}(RH), c_{eq}^{des}(RH), K_a, K_d, [c_{eq}(RH), RH_b, \kappa]_{i-1}, {}^{t-\Delta t}T, {}^tT)$$

$$\left[c_{eq}(\rho_v), \frac{\partial c_{eq}}{\partial \rho_v} \right]_i = f([c_{eq}(RH), \mathbf{a}]_i, {}^tT)$$

end of iteration loop

- accepting nodal values ${}^t\mathbf{a} = \mathbf{a}_i$

end of loop

Table 4.1: Constant element conductivity and stiffness matrices

	Referring to element equation	Referring to element function	at page number in appendix D
\mathbf{C}_{ap}^e	4.17	moist2i4e_C_ap	58
\mathbf{K}_{ac}^e	4.19	moist2i4e_K_ac	62
$\mathbf{K}_{\partial A_c}^e$	4.20	moist2i4e_K_dA	64
\mathbf{K}_{av}^e	4.21	moist2i4e_K_av	65
\mathbf{C}_{bc}^e	4.22	moist2i4e_C_bc	67
\mathbf{K}_{bc}^e	4.24	moist2i4e_K_bc	71

Table 4.2: Non-linear element stiffness matrices and residual vectors

	Referring to element equation	Referring to element function	at page number in appendix D
\mathbf{K}_{ai}^e	4.18	moist2i4e_K_ai_Q_ai	60
\mathbf{K}_{bi}^e	4.23	moist2i4e_K_bi_Q_bi	69
\mathbf{Q}_{ap}^e	4.25	-	
\mathbf{Q}_{ai}^e	4.26	moist2i4e_K_ai_Q_ai	60
\mathbf{Q}_{ac}^e	4.27	-	
$\mathbf{Q}_{\partial A_c}^e$	4.28	-	
\mathbf{Q}_{ext}^e	4.29	-	
\mathbf{Q}_{av}^e	4.30	-	
\mathbf{Q}_{bc}^e	4.31	-	
\mathbf{Q}_{bi}^e	4.32	moist2i4e_K_bi_Q_bi	69
\mathbf{Q}_{bc}^e	4.23	-	

4.3 Verification

Verification of the numerical formulation is presented in appendix B. It should be observed that this does not include the verification of the transport model.

Chapter 5

Finite element analysis

In the finite element analysis simulations are performed and compared to measurements in order to investigate the ability of the model. In the verification the vapor density ρ_v is evaluated inside a corrugated board box. The outside of the box is exposed to natural variation of temperature T_∞ and relative humidity RH_∞ .

5.1 Geometry

The box in figure 5.5 has the dimensions $0.4 \times 0.4 \times 0.4 \text{ m}^3$ and is made of a single wall corrugated board, 171C. The dimensions of the corrugated board is shown in figure 5.1. Assuming fast vapor diffusion in the air modelling one half of a wavelength, with thickness h , in two dimensions is sufficient to represent the whole box. The air body inside the box is considered by meshing air elements with decreasing thickness unto the middle of the box. The thickness h [mm] is defined according to equation (5.1). The complete mesh can be seen in figure 5.2.

$$\begin{aligned} h(x) &= \left(\frac{x}{188.5} \right)^2 & (x < 188.5) \\ h(x) &= 1 & (x \geq 188.5) \end{aligned} \quad (5.1)$$

The assumption of fast vapor diffusion in the air will later be proven correct.

5.2 Boundary conditions

The finite element mesh is demarcated with two types of boundaries; the outside of the box with a convection boundary condition (essential boundary condition), and at the other boundaries the flux of vapor is zero, (natural boundary condition).

The air in the cells between the sheets of the board and in the air body inside of the box is assumed to be still. The outcome of this assumption is that no convective layer in the internal transition between paper and air elements exists, i.e. the vapor density is continuous here.

5.3 Material modelling

The material is assigned isotropic characteristics, see section 2.1. The boundary sorption curves c_{eq}^{ads} and c_{eq}^{des} for the liner material Whitetop 200 [g/m²] are referred to chapter 3 and are assumed to hold for all layers of the board. The remaining material properties are given in table 5.1.

Table 5.1: Material properties used in simulations.

ε_v	0.54	[5]
D_v [m ² /s]	2.95×10^{-8}	[3]
D_a [m ² /s]	25×10^{-6}	[6]
k_c [1/s]	7.67×10^{-3}	[3]
k_b [m/s]	4.31×10^{-3}	[3]
ρ_p [kg/m ³]	748	[4]

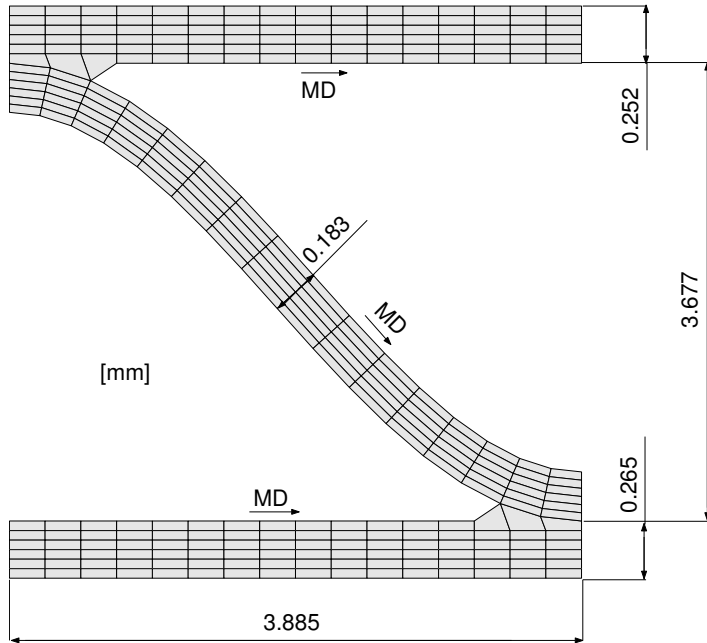


Figure 5.1: Dimensions of the corrugated board

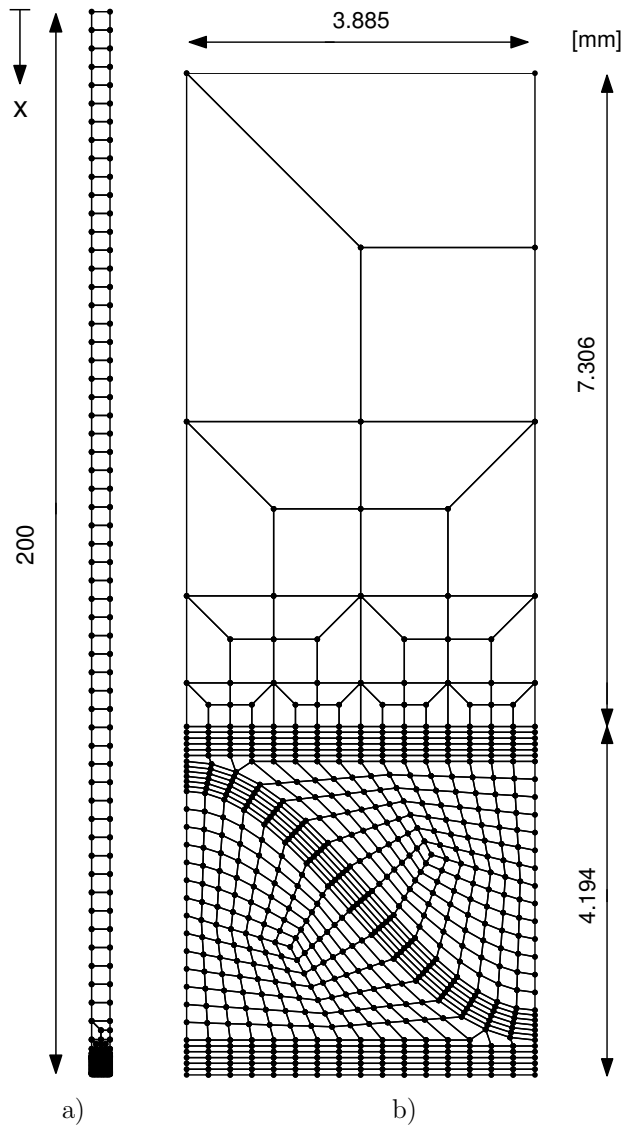


Figure 5.2: a) Complete mesh. b) Enlargement of the lower part of figure a

5.4 Introductory simulations

As a first step the model is investigated in the following order. The material is assumed to be completely dry. The exterior boundary at the outer liner is then subjected to a rapid change in RH to 90 %. The temperature is held constant. Simulated RH is shown every 30 minutes in figure 5.3 and 5.4.

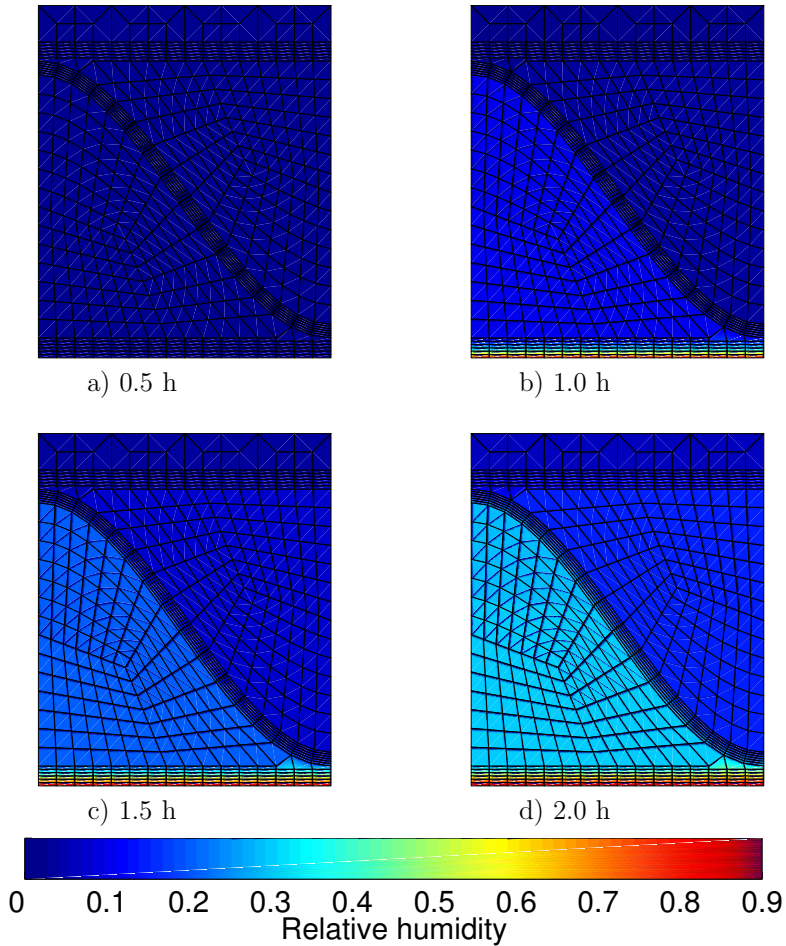


Figure 5.3: Development of relative humidity

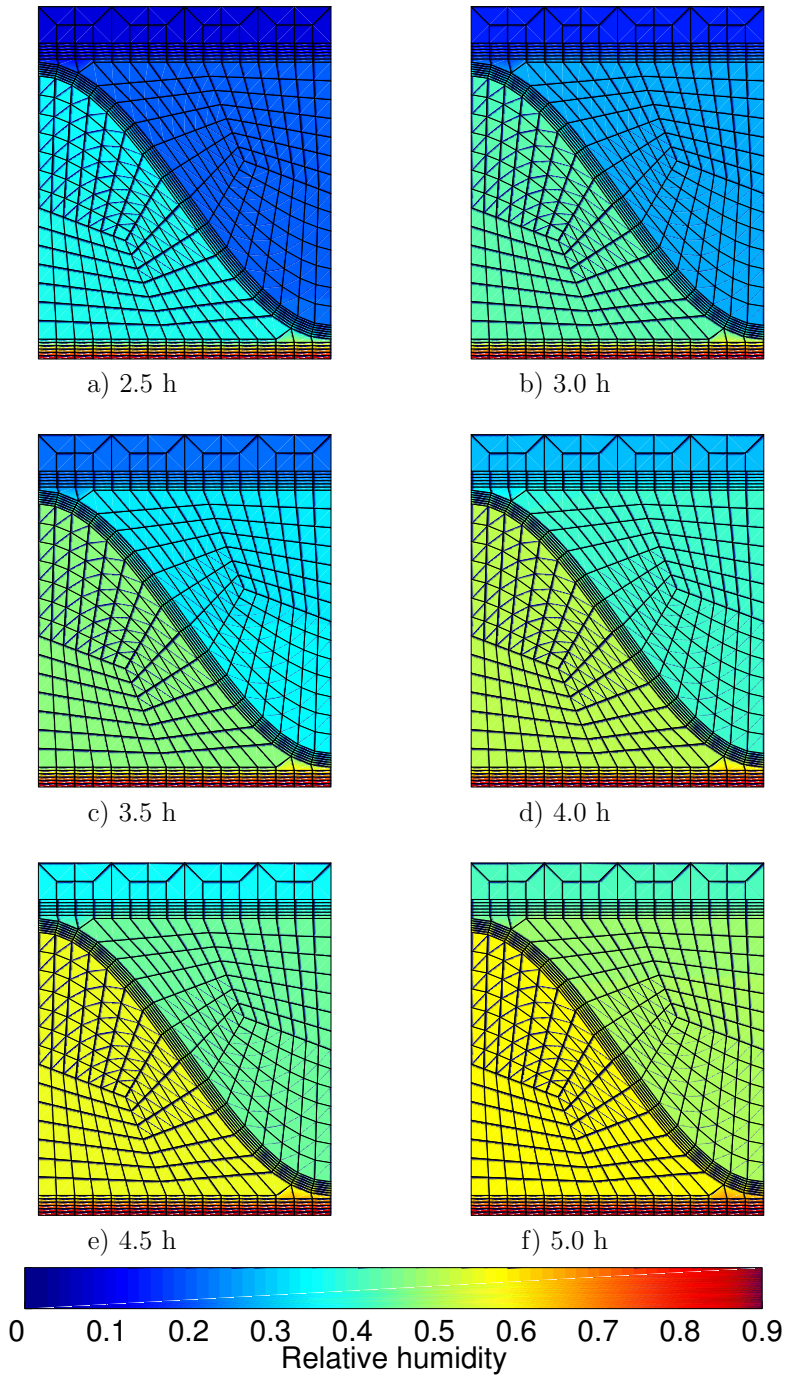


Figure 5.4: Development of relative humidity

5.5 Climate measurements

Edges and slits are sealed with tape on the corrugated board box and measurements of relative humidity RH and temperature T are performed externally and internally throughout one year. The test arrangement can be seen in figure 5.5. The scales inside and outside of the box are used in other experiments and have nothing to do with the climate measurements.

The measurement data is noisy and the elapsed time between each measurement is irregular. In order to represent RH and T in a fashion suitable for the incremental procedure vectors adjusted to fit the time step Δt in the simulation are produced by linear interpolation. The noise in the data is then reduced by using temporal averages.

The relative humidity outside the box RH_∞ before and after the transformation can be seen in figure 5.6. The ticks on the x-axis correspond to midnight.

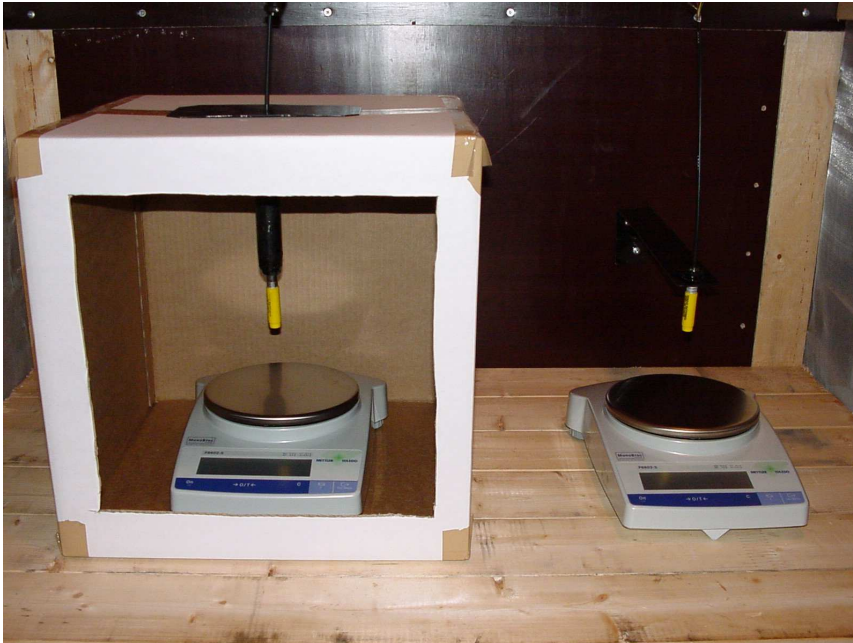


Figure 5.5: Test arrangement

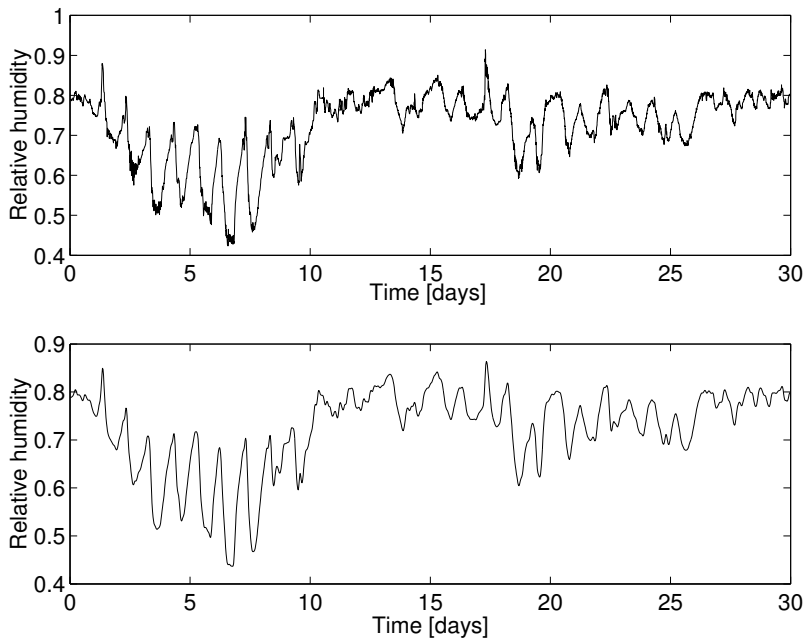


Figure 5.6: Relative Humidity outside the box, upper diagram shows measurements, lower diagram shows transformed data suited to the simulation

5.6 Simulations

The simulations are carried out for June 2002. The climate during this period is fluctuating to a large extent and provide satisfying conditions in order to test the ability of the model. Figure 5.7 shows the simulated RH inside the box compared to the measured.

Periods of special interest are then examined in detail by presenting RH , vapor density ρ_v and T as they are related to each other.

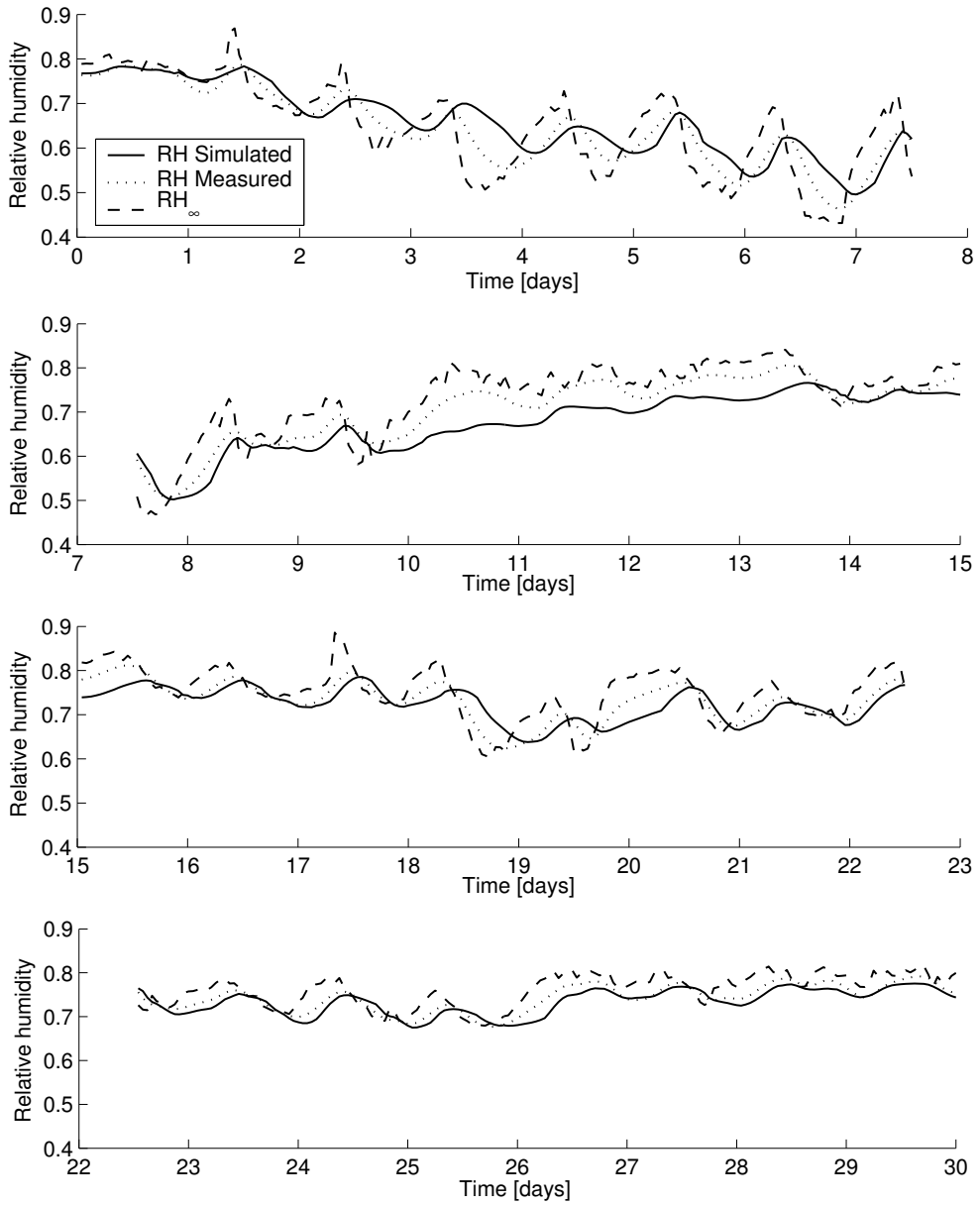


Figure 5.7: Relative humidity in June

For the period from day 2 to 8 the daily climate fluctuation is regular see figure 5.8. It is seen that interior RH level lags the exterior RH by 4-6 hours. It is also noted that the peak to peak values of the interior RH level is decreased by approximately 10 % units compared to the exterior peak to peak values. For this time period the resemblance between simulated level and measured level reasonably fair.

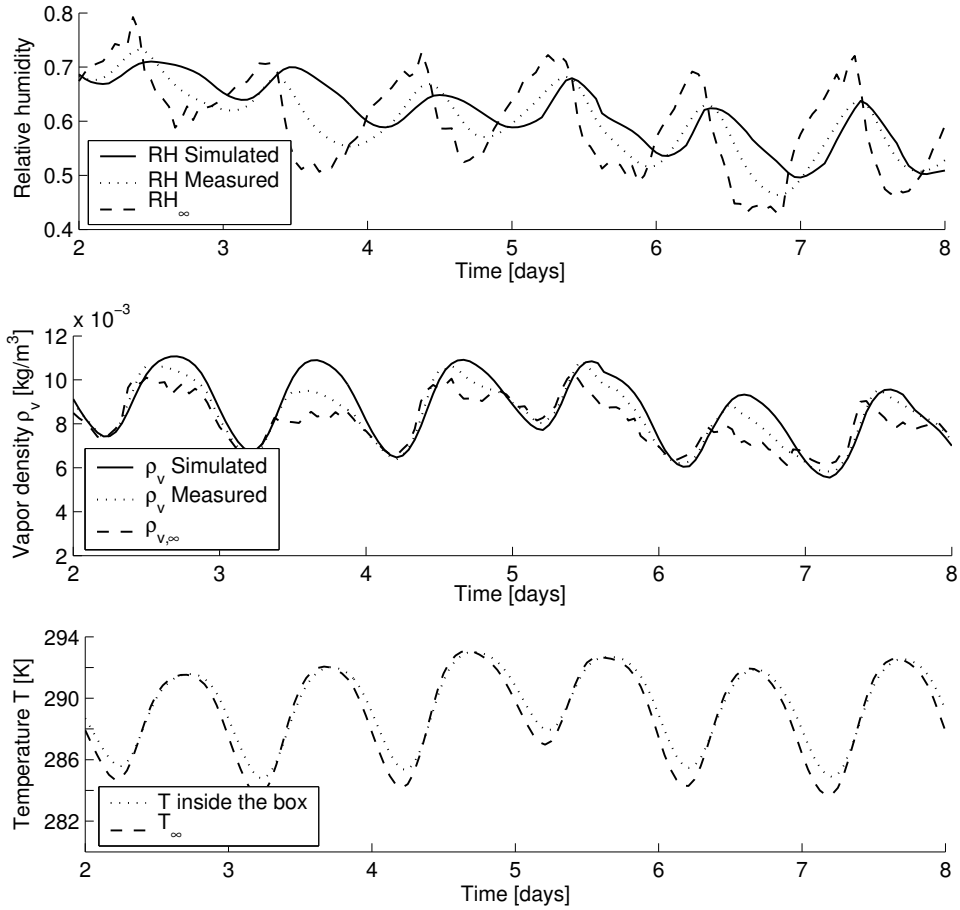


Figure 5.8: Period from day 2 to 8

For the period from day 10 to 16, figure 5.9, the simulated RH is lower than the measured. Furthermore, the phase-shift is in this case not apparent.

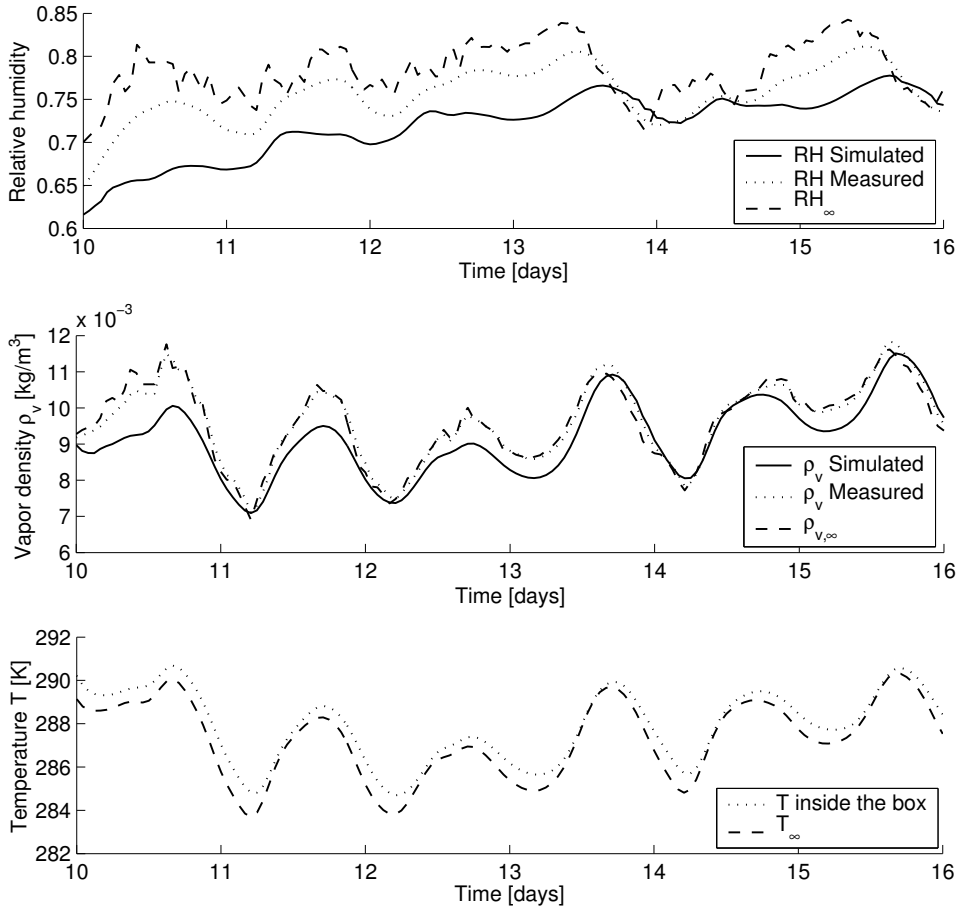


Figure 5.9: Period from day 2 to 8

In figure 5.10 the development of RH in different nodes are presented in the same plot. The green lines corresponding to air nodes are very close, which indicate fast diffusion in the air. The blue lines correspond to the paper nodes.

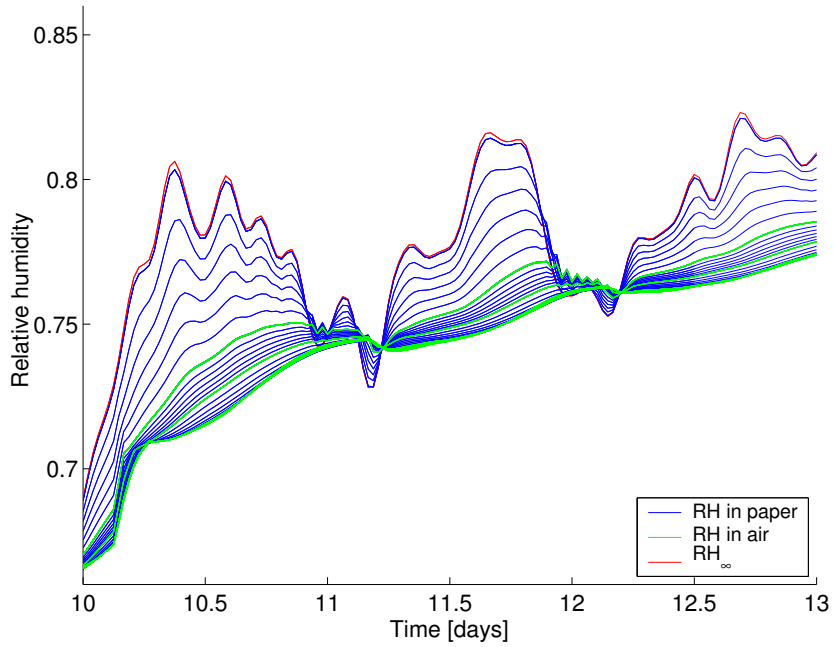


Figure 5.10: Development of relative humidity in different nodes

Chapter 6

Neutron radiography

6.1 Summary

Herein the method of neutron radiography is used to measure the transient moisture content over sections of corrugated board. The purpose of this is to achieve detailed data regarding the moisture transport in paper, for comparison to calculated results and verification of the two-dimensional FE-model.

For the chosen geometry, the amount of water to be detected is small compared to the variance due to certain characteristics in the detection system. Therefore the water uptake is difficult to see. Furthermore, moisture leakage occurs between the seal and the edge of the board.

Another phenomena causing problems is that the samples deform due to hygroexpansion during the water uptake. It can be concluded that in future tests the depth of the specimens should be larger than in the current test, in order to increase the attenuation of the neutron beam compared to the variance in the detection system. In addition the seals on the edges need to be improved.

6.2 NEUTRA

NEUTRA (NEUtron Transmission RAdiography) is an equipment available at Paul Scherrer Institute (PSI) in Villigen, Switzerland. A neutron transmission radiography setup consists of a neutron source, a collimator guiding the neutrons to the object under investigation and an area neutron detector collecting the transmitted neutrons behind the sample. The neutron detector measures the intensity of the attenuated beam along lines through the sample providing a two dimensional description of its neutron transmission characteristics. A schematic representation of this is shown in figure 6.1.

The applications are many, e.g. in material science (defect detection, homogeneity in composite materials, alloys), in biology (plants, fossil specimens) and in civil engineering (analysis of moisture content, effectiveness of impregnating agents in different building materials).

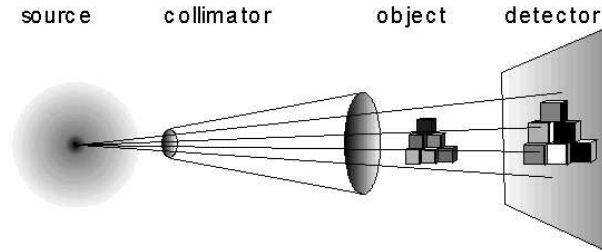


Figure 6.1: Principle of the neutron radiography

Different nucleus have different capability to absorb and interact with free neutrons. For example aluminium affects neutrons very little, while hydrogen has a much higher probability of absorbing the neutrons, which is quantified in the attenuation coefficient. This implies that water content can be detected, which is the purpose in these experiments.

Figure 6.2 shows the principal components of the radiography facility. Neutrons are generated in the target, a lead rod, when subjected to high energy proton irradiation. The neutrons are slowed down to a certain energy level when passing surrounding heavy water in the moderator tank. A straight pipe guides the neutrons to the sample position.

In order to form a suitable parallel neutron field for radiography purposes, the beam is guided in a first converging and then diverging collimating pipe.

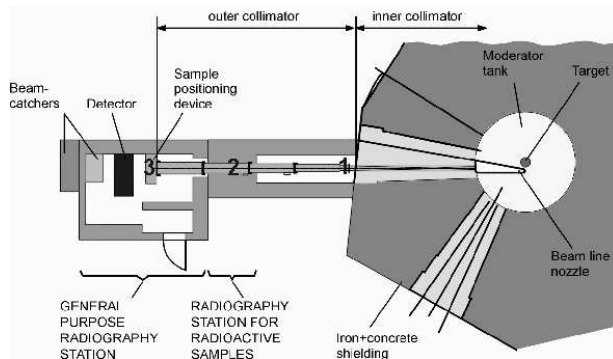


Figure 6.2: Layout of the thermal neutron radiography facility NEUTRA at the PSI spallation source

Detection is in our case carried out using a digital camera system that registers the light emitted from a ${}^6_3\text{Li}$ doped scintillator when absorbing the neutrons. This detector system provides a relatively high spatial resolution (0.053 mm). One picture consists of 1024×1024 pixels, which corresponds to $5 \times 5 \text{ cm}^2$. Each pixel contains a numerical value of the neutron intensity \tilde{I} .

Due to variation of the composition of the light emitting substance, ${}^6_3\text{Li}$, in the scintillator and the fact that the beam is quasi parallel the pictures become somewhat inhomogeneous. These imperfections are reduced by division with a picture without any object in the beam $I_{open\ beam}$ (open beam picture).

$$I = \frac{\tilde{I}}{I_{open\ beam}} \quad (6.1)$$

Because of fluctuating beam intensity a normalization with respect to the intensity outside the sample is carried out according to following expression.

$$\frac{I}{I_o} = e^{-(\Sigma_p + \Sigma_w) \cdot t} \quad (6.2)$$

I_o Detected neutron intensity outside the sample

I Detected neutron intensity within the area of the sample

t Depth of the the sample in beam direction [cm]

Σ_p Coefficient describing the neutron absorption due to paper and testing equipment in the beam line [cm^{-1}]

Σ_w Coefficient describing the neutron absorption due to water [cm^{-1}]

$$\Sigma_w = \frac{\rho_w \cdot N_A}{M_w} \cdot \mu \quad (6.3)$$

ρ_w Water content [g/cm^3]

$N_A = 6.022 \cdot 10^{23} \text{ mol}^{-1}$ Avogadros constant

$M_w = 18.01 \text{ g/mol}$ Molecular mass of water

$\mu = 30 \cdot 10^{-24} \text{ cm}^2$ Attenuation coefficient

6.3 Description of the tests

Before the actual testing started the samples are preconditioned and conditioned. The preconditioning occurs at 20 % RH , 23 °C in 48 h. The conditioning occurs at 33 % or 85 % RH , 20 °C which are the initial conditions for the tests.

A climate chamber is used to control the relative humidity during the tests. The climate chamber can provide either equal RH on both sides of the sample or different levels of RH on each side.

6.3.1 Test A

Moisture uptake, single wall corrugated board

This test measures the transient moisture uptake on a 4 mm thick single wall corrugated board. The RH is equal on both sides of the board. The specimen, 5 mm deep in beam direction, is initially in equilibrium with 33 % RH . It is subjected to 85 % RH during the test. The test extends over 892 minutes and a picture is taken every 15 minutes. The sample moves and swells during the moisture uptake and the amount of water change is too small in order to give enough contrast in the pictures. The only thing that can be detected is the movement and not the actual water uptake.

6.3.2 Test B

In plane moisture uptake

The purpose of this test is to examine the orthotropy of diffusivity in the material. The two specimens are 2 mm wide paper strips and 0.8 mm thick (in beam direction). Initially the specimens are in equilibrium with 33 % RH and subjected to 85 % RH during the test. The transient diffusion is parallel with machine direction in one of the strips and perpendicular to machine direction in the other. The change of water content was not possible to detect in this test.

6.3.3 Test C

Contrast test

The purpose of this test is to examine the contrast between initially moist and completely dried samples. The specimens are made of cardboard strips 10 mm wide. The beam direction is perpendicular to the plane of the board. Images are first produced for the moist specimens (33 % and 85 % RH). Then the specimens are dried in an oven at 103 °C and new images are produced for the dry specimens.

Specimen 1: 3.75 mm thick hand made paper, in equilibrium with 33 %.

Specimen 2: 0.8 mm thick paper, in equilibrium with 33 %.

Specimen 3: 0.8 mm thick paper, in equilibrium with 85 %.

Table 6.1: Result of the contrast test, weighed versus detected water content

Specimen	Initial RH	Detected water content [g/cm ³]	Σ_w [cm ⁻¹]	Weighed water content [g/cm ³]
1	33 %	0.0677	0.0679	0.028
2	33 %	0.0914	0.0918	0.037
3	85 %	0.1099	0.1103	0.067

The different images of the moist and dry specimens show a significant contrast. Figure 6.3 shows the calculated change in water density compared to the weighed value, for the three homogenous specimens.

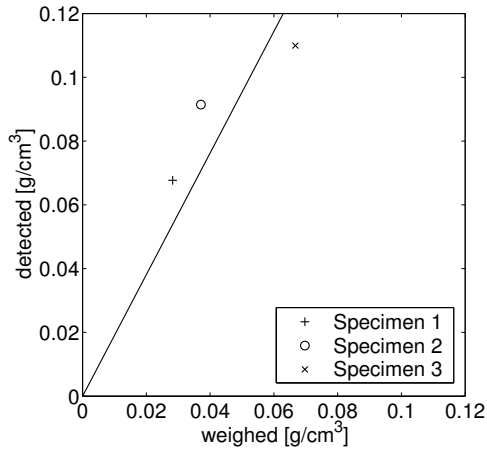


Figure 6.3: Weighed versus detected water content

Even though the values do not fit a straight line with the slope of 45°, which they ideally should do. With only three specimens the reliability of the fitted line is poor. However, the result indicates that a significant change in moisture content has been detected. Therefore it is decided to carry out another experiment, Test D, with samples of increased dimensions under a relatively long time.

6.3.4 Test D

Moisture uptake, triple wall corrugated board

The specimen consists of 12 mm thick triple wall corrugated board with liner thickness 0.5 mm, see figure 6.7. The depth of the specimen is 15 mm in beam direction. The conditioning occurs at 33 % *RH*. The climate on the right-hand side is kept constant at 85%, whereas the left-hand side climate is ventilated with air at 15 %. Due to leakage the relative humidity is initially 33 % and increases to 60 % during the test, see figure 6.4. The moisture distribution of water will thereby reach steady state condition in the interval 60 - 85 % *RH*, where the slope of the sorption isotherm is very steep.

An image is taken every 15 minutes and the test extends over 3660 minutes, which is estimated as sufficient time in order for the transient moisture distribution to develop into steady state condition.

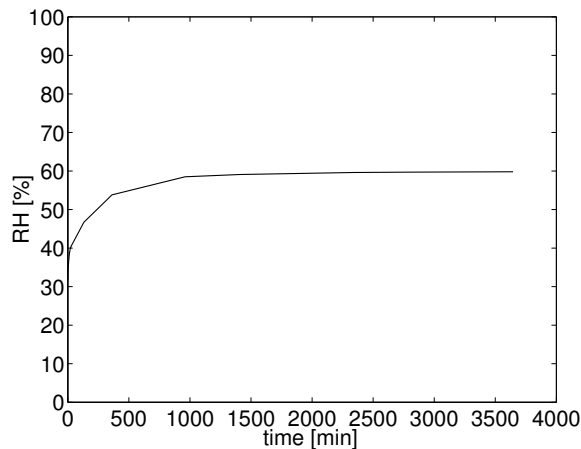


Figure 6.4: Development of climate in internal chamber

Result of Test D

The pixel intensity values show large variability, and it is difficult to distinguish the change of moisture. However, the following two approaches are made in this purpose.

As a first approach, using the image processing program Image Pro Plus, provided by the PSI, the pictures at the points of time 35 min, 93 min, 128 min, 257 min, 568 min, 1993 min and 3660 min are evaluated. First a correction due to imperfections in the scintillator is performed, by taking an open beam picture into consideration. By normalizing and integrating in machine direction, the intensity profiles, in the right and the left liner are created, see figure 6.5.

The movement of the samples is considered by shifting the pixels until the intensity minimum values coincide. The normalized intensity profiles are then referred to the mean value of the first four pictures, in order to get profiles only due to change of water content, figure 6.6. Insertion of $\frac{I}{I_0}$ into equation (6.2) provides the moisture uptake $\Delta\rho_w$.

The amount of water to be detected is very small. The intensity in figure 6.5 hardly vary at all. The referred profiles in figure 6.6b therefore do not reflect the change in moisture content in a proper way. The systematic behavior in figure 6.6a is likely to depend on movement, which could not be compensated for entirely.

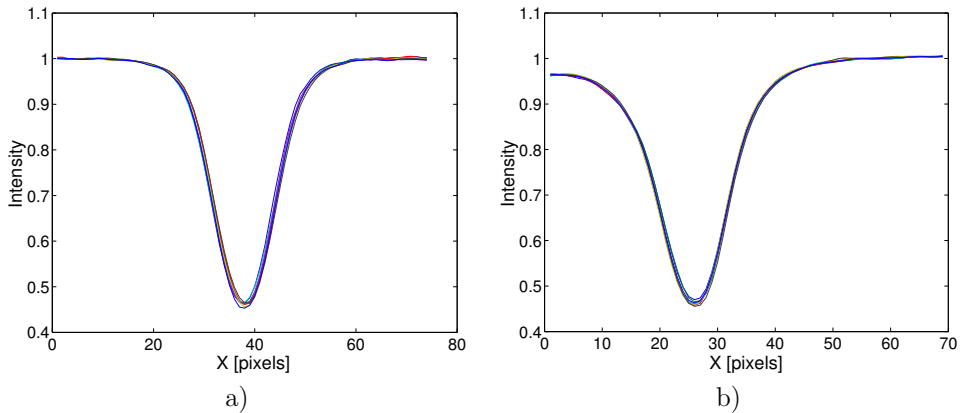


Figure 6.5: Normalized intensity profile. a) Left liner. b) Right liner

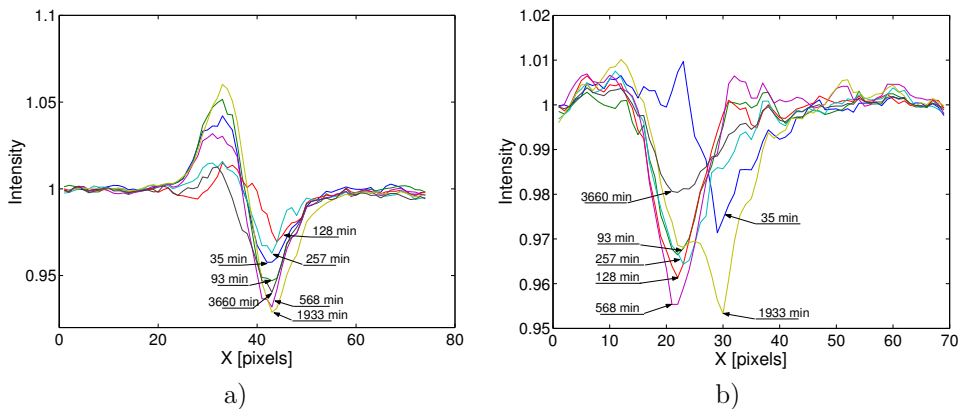


Figure 6.6: Intensity profile referred to initial picture. a) Left liner. b) Right liner

As a second approach all the pictures are evaluated in MATLAB. Open beam correction and reference to the first picture are done. The moisture content in certain areas of interest (figure 6.7) are integrated in order to achieve a mean value of the water uptake in all four liners for each time.

The left liner as well as the right (figure 6.8), show increasing moisture uptake, which seems reasonable. The inner liners (figure 6.9) do not show anything at all.

The indistinct outcome of the experiment makes it difficult for the results to be compared to the FE-simulation.

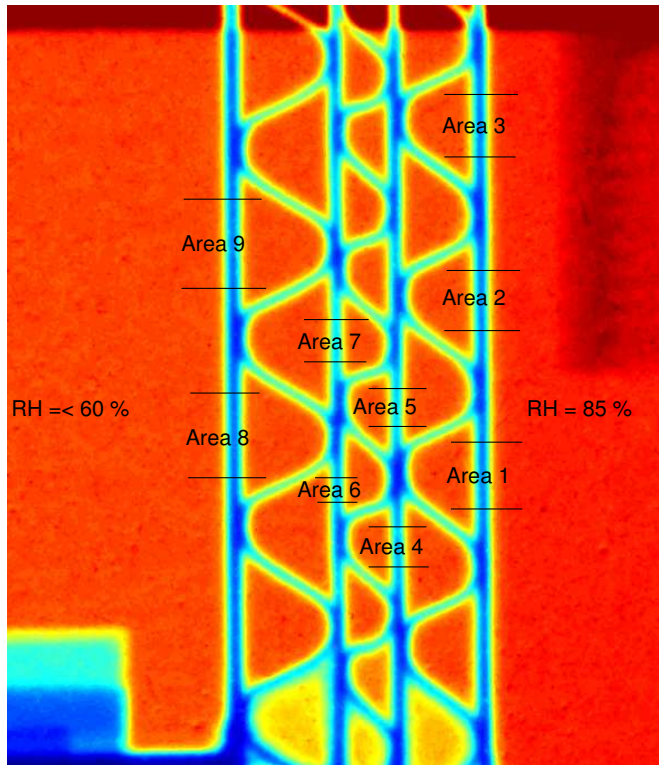
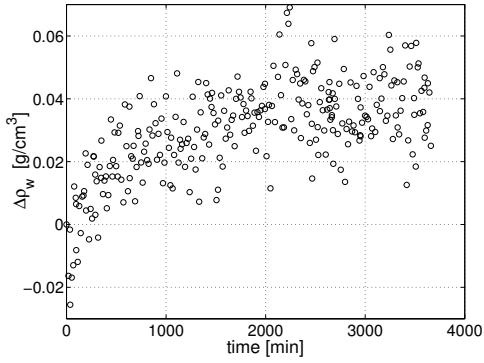
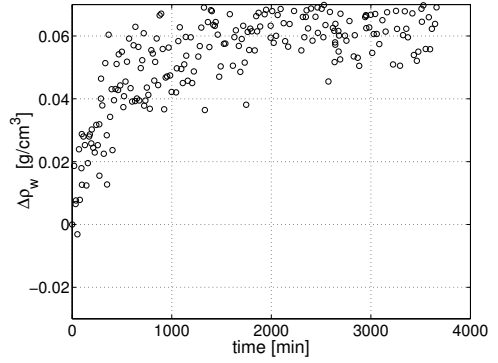


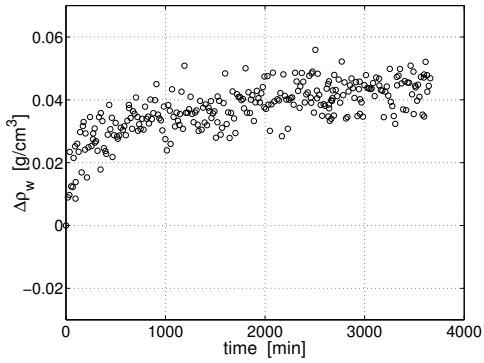
Figure 6.7: Integration areas in board section



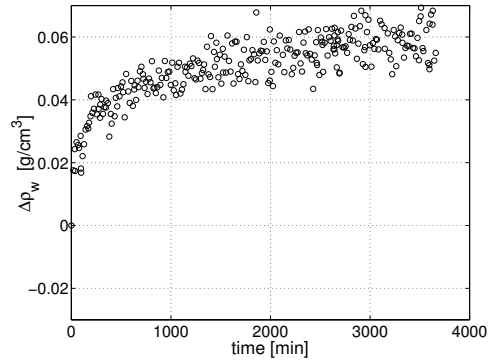
a) Left liner, area 8



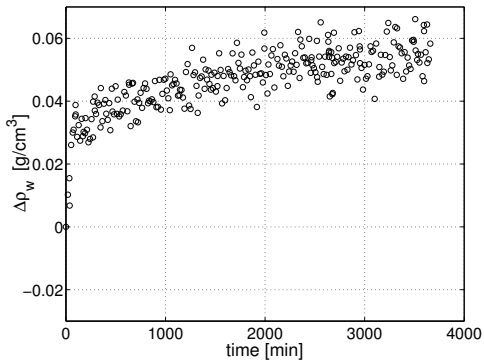
b) Left liner, area 9



c) Right liner, area 1

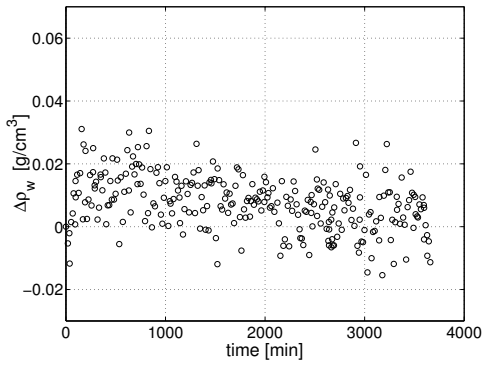


d) Right liner, area 2

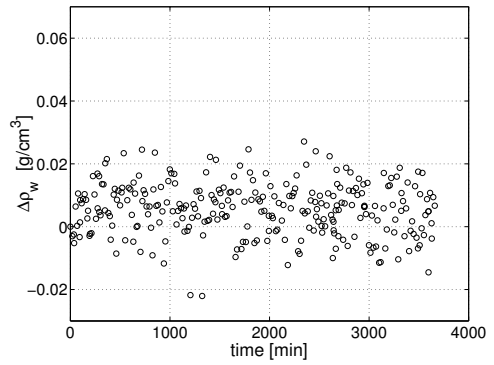


e) Right liner, area 3

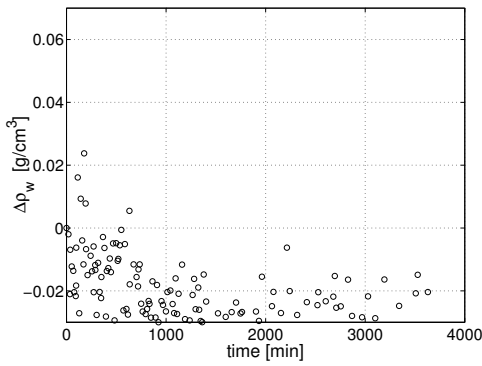
Figure 6.8: Water uptake in the outer liners.



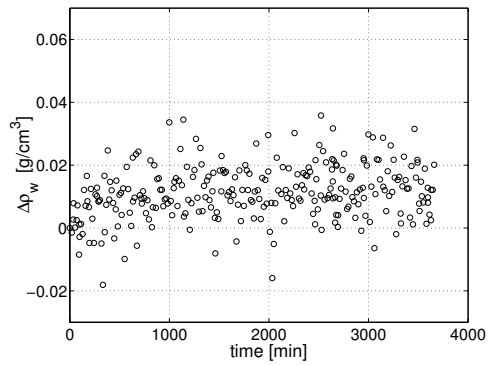
a) Inner right liner, area 4



b) Inner right liner, area 5



c) Inner left liner, area 6



d) Inner left liner, area 7

Figure 6.9: Water uptake in the inner right and inner left liners.

Chapter 7

Concluding remarks

7.1 Conclusions

The developed two-dimensional FE-model is capable of simulating moisture dynamics due to climate fluctuations. The verification of the model is made with respect to vapor density. Moisture concentration profiles were intended to be compared to the measurements performed at the PSI in Switzerland using neutron radiography spectroscopy. However, this part of the verification failed.

It can be established that the assumption of fast vapor transport in the air is correct. The vapor density is approximately equal in the whole air body inside the box. Furthermore, the diffusion occurs almost exclusively perpendicular to the paper sheets. Regarding these facts a one-dimensional geometric model would be sufficient in order to represent an empty box.

However, with a more complex moisture movement, the necessity of the two-dimensional model is obvious. This could be the case if the box contains a material with not negligible diffusive resistance.

7.2 Possible improvements of the model

In order to deal with the latent heat of condensation it is possible to include thermodynamic coupling with the temperature as a nodal value. The problem then also includes heat conduction.

Implementation of the hysteresis effect is based on sound assumptions but can not be regarded as indubitable. Sophisticated measurements might improve the accuracy of these assumptions.

In the simulation isotropy is implemented and the diffusion occurs almost exclusively perpendicular to the sheet's plane. In case of significant orthotropy this might not correspond to the real behavior. Performing detailed experiments in order to investigate orthotropic diffusivity properties might improve the model.

Bibliography

- [1] Allansson A. and Svärd B. *Stability and Collaps of Corrugated Board* Division of Structural Mechanics, Lund University, Lund 2001.
- [2] Edlind N. *Modelling and Visualization of the Geometry of Fibre Materials* Division of Structural Mechanics, Lund University, Lund 2003.
- [3] Hägglund R, Westerlind B, Gulliksson M, Nordstrand T. *Diffusion of Water Vapor in Paper* Fundamental Advances in the Pulp and Paper Industry, AIChE Symposium Series No. 322, Vol 95, pp 71-79, 1999
- [4] Nyman U. and Gustafsson P.J. *A Numerical Method for the Evaluation of Non-linear Transient Moisture Flow in Cellulosic Materials* Division of Structural Mechanics, Lund University, Lund 2003.
- [5] Ramarao B.V. *Moisture Sorption and Transport processes in Paper Materials* Empire State Paper Research Institute SUNY Collage of Environmental Science and Forestry Syracuse, New York 1998.
- [6] Sandin K. *Värme och Fukt* Lunds Tekniska Högskola, Institutionen för byggnadsteknik, Byggnadsfysik, Lund 1996.
- [7] Scandinavian pulp, paper and board; Testing committee *Fukt i papper och papp* SCAN -P 4:63, 1962.

Appendix A

Sorption, numerical values

Table A.1: 200WT, adsorption

RH	c_{eq} [kg/kg] Sample 1	c_{eq} [kg/kg] Sample 2	c_{eq} [kg/kg] Sample 3	c_{eq} [kg/kg] Sample 4	c_{eq} [kg/kg] Sample 5	c_{eq} [kg/kg] Sample 6
0.0	0.0000	0.0000	0.0000	0.0000	0.0000	0.0000
0.19	0.0441	0.0448	0.0440	0.0466	0.0459	0.0468
0.30	0.0496	0.0494	0.0488	0.0522	0.0513	0.0518
0.40	0.0604	0.0608	0.0592	0.0632	0.0622	0.0620
0.49	0.0711	0.0712	0.0703	0.0741	0.0729	0.0732
0.59	0.0831	0.0834	0.0824	0.0869	0.0856	0.0860
0.69	0.0987	0.0989	0.0976	0.1023	0.1009	0.1007
0.77	0.1222	0.1212	0.1202	0.1248	0.1232	0.1221
0.92	0.1868	0.1929	0.1942	0.1887	0.1913	0.1944

Table A.2: 200WT, desorption

RH	c_{eq} [kg/kg] Sample 1	c_{eq} [kg/kg] Sample 2	c_{eq} [kg/kg] Sample 3	c_{eq} [kg/kg] Sample 4	c_{eq} [kg/kg] Sample 5	c_{eq} [kg/kg] Sample 6
0.92	0.2303	0.2325	0.2365	0.2399	0.1810	0.1825
0.77	0.1488	0.1491	0.1492	0.1532	0.1393	0.1396
0.69	0.1237	0.1241	0.1236	0.1273	0.1195	0.1198
0.59	0.1052	0.1058	0.1047	0.1082	0.1034	0.1034
0.49	0.0892	0.0897	0.0883	0.0921	0.0887	0.0887
0.40	0.0746	0.0752	0.0741	0.0777	0.0747	0.0750
0.30	0.0613	0.0618	0.0609	0.0642	0.0623	0.0626
0.19	0.0479	0.0487	0.0480	0.0514	0.0500	0.0503
0.0	0.0000	0.0000	0.0000	0.0000	0.0000	0.0000

Samples 1, 2, 3 and 4 are soaked. Samples 5 and 6 are left in 92 % RH until desorption starts.

Mean values, μ , and standard deviation, σ , of the measurements for the adsorption, desorption and interior desorption are presented in table A.3.

Table A.3: 200WT, desorption

RH	c_{eq}^{ads}	c_{eq}^{ads}	c_{eq}^{des}	c_{eq}^{des}	c_{eq}^{int}	c_{eq}^{int}
	[kg/kg]	[kg/kg]	[kg/kg]	[kg/kg]	[kg/kg]	[kg/kg]
	μ	σ	μ	σ	μ	σ
0.0	-	-	-	-	-	-
0.19	0.0454	0.0012	0.0490	0.0016	0.0502	0.0002
0.30	0.0505	0.0014	0.0620	0.0015	0.0625	0.0002
0.40	0.0613	0.0014	0.0754	0.0016	0.0749	0.0002
0.49	0.0721	0.0015	0.0898	0.0016	0.0887	-
0.59	0.0846	0.0018	0.1060	0.0016	0.1034	-
0.69	0.0998	0.0017	0.1247	0.0018	0.1197	0.0002
0.77	0.1223	0.0016	0.1501	0.0021	0.1395	0.0002
0.92	0.1914	0.0031	0.2348	0.0043	0.1817	0.0011

Appendix B

Verification of the numerical formulation

Verification of the two-dimensional isoparametric element equations is carried out in two steps. Firstly, a comparison between an analytical and a numerical FE solution with one-dimensional elements [4] is carried out. Secondly, a comparison between two numerical solutions, one-dimensional elements versus two-dimensional isoparametric elements, chapter 4, is performed.

B.1 Analytical versus one-dimensional

The analytical solution is based on the transport model in section 2.1, with the following simplifications; fast transport between pore vapor and fibre liquid phase (8.1) and equilibrium moisture concentration in fibre phase is linear dependent of the vapor density (8.2). The analytical solution is expressed as a sum of trigonometric functions with a limited number of terms. The complete derivation is presented in appendix C.

$$\frac{\partial c_l}{\partial t} \approx \frac{\partial c_{eq}}{\partial t} \quad (8.1)$$

$$\frac{\partial c_{eq}}{\partial \rho_v} = \text{constant} \quad (8.2)$$

In order to achieve the same conditions for the numerical and analytical solution the assumptions (8.1) and (8.2) are also implemented in the numerical solution. To further improve the agreement the paper section (thickness 0.285 mm) is modelled with very small elements, totally a 100 elements. A comparison between analytically and numerically calculated moisture profiles is then carried out with respect to the following (initial and boundary) conditions. The paper is initially in equilibrium with 90 % *RH*, which corresponds to $\rho_v = 0.0156 \text{ kg/m}^3$ at $T = 20^\circ\text{C}$. After initiation the paper sheet is exposed to an exterior climate with 0 % *RH* and the development of the moisture profiles are evaluated.

The result can be seen in figure B.1. The results of the two different methods are nearly identical.

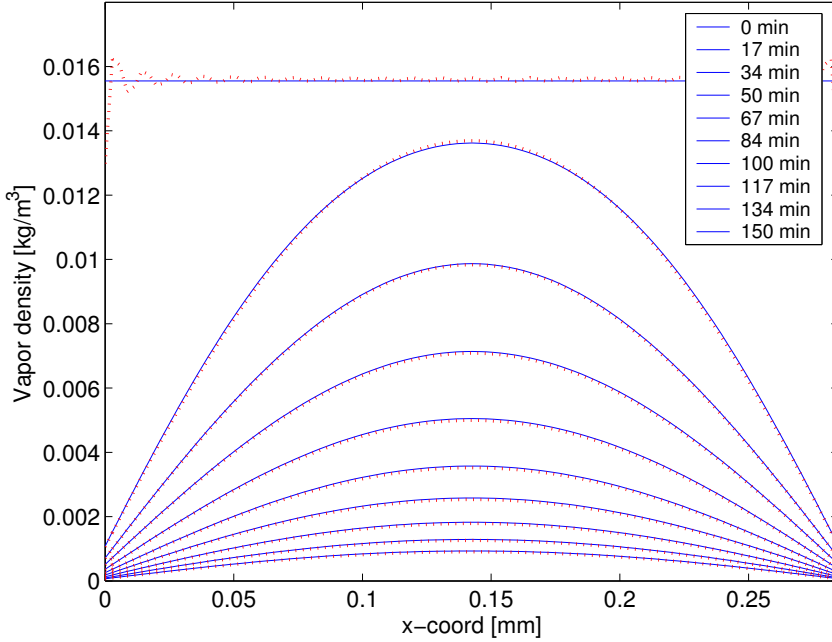


Figure B.1: Comparison of analytical and one-dimensional numerical solution. Dashed line (red): analytical, Solid line (blue): numerical

B.2 One-dimensional versus two-dimensional

A comparison between one- and two-dimensional simulations of vapor density in a single paper sheet, with thickness 0.285 mm, is performed with respect to the following conditions. The paper sheet is initially in equilibrium with 20 % RH which corresponds to $\rho_v = 0.0041 \text{ kg/m}^3$ at $T = 23^\circ\text{C}$. An impermeable layer (symmetry line) covers one side of the paper sheet and the other side is exposed to an exterior climate with 30 % RH which corresponds to $\rho_v = 0.0062 \text{ kg/m}^3$ at $T = 23^\circ\text{C}$.

The two-dimensional distorted mesh and points of evaluation is shown in figure B.2. The first evaluation point is placed in the center of the mesh and the second point is placed on the symmetry line. The results of the one-dimensional and two-dimensional case, presented in figure B.3, are identical which verifies the two-dimensional isoparametric element equations.

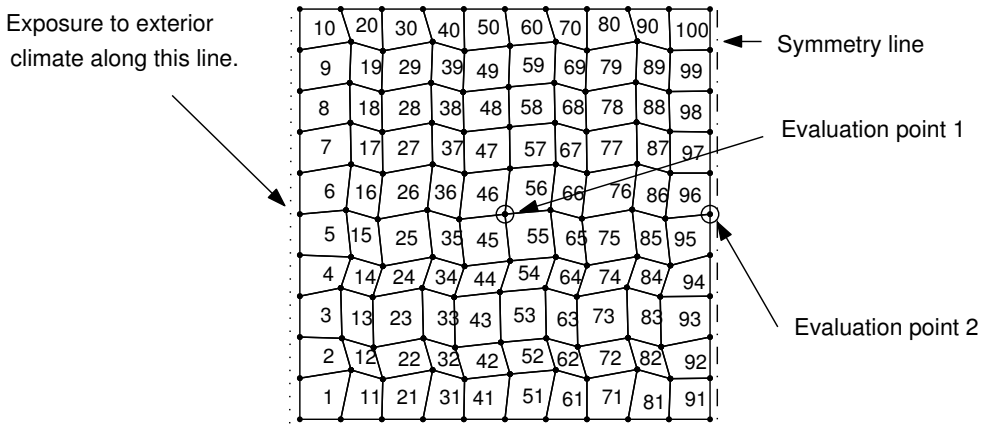


Figure B.2: Isoparametric mesh used in the comparison, evaluation points are marked with 'o'

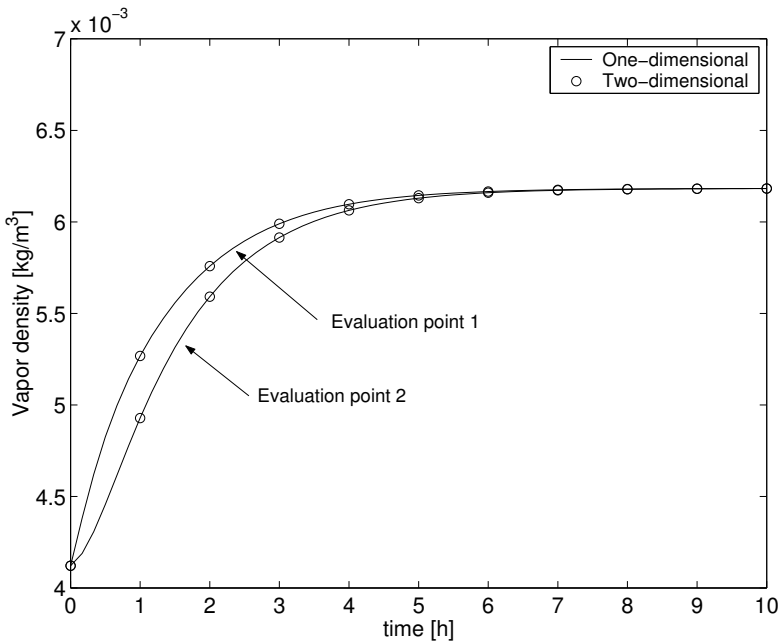


Figure B.3: Development of vapor density in evaluation points

Appendix C

Analytical solution

Transport model according to section 2.1 equation (2.6) boundary conditions according to equation (2.7) with additional boundary condition at $x = 0$.

$$\varepsilon \dot{\rho}_v + \rho_s \dot{c}_l = D_v \frac{\partial^2 \rho_v}{\partial x^2}, \quad 0 < x < L, \quad t > 0 \quad (9.1)$$

$$\left. \frac{d\rho_v}{dx} \right|_{x=0} = \gamma [\rho_v - \rho_{v,\infty}]_{x=0}, \quad \gamma = \frac{k_b}{D_v} \quad (9.2)$$

$$\left. \frac{d\rho_v}{dx} \right|_{x=L} = -\gamma [\rho_v - \rho_{v,\infty}]_{x=L} \quad (9.3)$$

Use the chain rule to obtain

$$\dot{c}_l = \frac{\partial c_l}{\partial \rho_v} \frac{\partial \rho_v}{\partial t} = f'(\rho_v) \frac{\partial \rho_v}{\partial t} \quad (9.4)$$

Assume fast transport between pore and fibre phase

$$\frac{\partial c_l}{\partial t} \approx \frac{\partial c_{eq}}{\partial t} \Rightarrow f'(\rho_v) \approx \frac{\partial c_{eq}}{\partial \rho_v} \quad (9.5)$$

(9.1), (9.4), and (9.5) results in the differential equation

$$(\varepsilon + \rho_s f'(\rho_v)) \frac{\partial \rho_v}{\partial t} - D_v \frac{\partial^2 \rho_v}{\partial x^2} = 0 \quad (9.6)$$

Divide ρ_v into a stationary and a transient part

$$\rho_v(x, t) = \rho_{v,st}(x) + \rho_{v,tr}(x, t) \quad (9.7)$$

The stationary problem is given by

$$\frac{\partial^2 \rho_{v,st}}{\partial x^2} = 0, \quad 0 < x < L \quad (9.8)$$

$$\left. \frac{\partial \rho_{v,st}}{\partial x} \right|_{x=0} = \gamma [\rho_{v,st} - \rho_{v,\infty}]_{x=0}, \quad t > 0 \quad (9.9)$$

$$\left. \frac{\partial \rho_{v,st}}{\partial x} \right|_{x=L} = -\gamma [\rho_{v,st} - \rho_{v,\infty}]_{x=L}, \quad t > 0 \quad (9.10)$$

The stationary problem is fulfilled by a partial solution

$$\rho_{v,st} = \frac{1}{\gamma L + 2} ((\gamma x + 1) [\rho_{v,\infty}]_{x=L} + (1 + \gamma L - \gamma x) [\rho_{v,\infty}]_{x=0}) \quad (9.11)$$

Make use of (9.7) $\rho_v = \rho_{v,st} + \rho_{v,tr}$ and (9.11)

$$\frac{\partial \rho_v}{\partial t} = \frac{\partial \rho_{v,tr}}{\partial t}, \quad \frac{\partial^2 \rho_v}{\partial x^2} = 0 + \frac{\partial^2 \rho_{v,tr}}{\partial x^2} \quad (9.12)$$

$$\frac{\partial \rho_v}{\partial x} = \frac{\partial \rho_{v,st}}{\partial x} + \frac{\partial \rho_{v,tr}}{\partial x} = \frac{\gamma([\rho_{v,\infty}]_{x=L} - [\rho_{v,\infty}]_{x=0})}{\gamma L + 2} + \frac{\partial \rho_{v,tr}}{\partial x} \quad (9.13)$$

$$\rho_v(0, t) = \rho_{v,st}(0) + \rho_{v,tr}(0, t) = \quad (9.14)$$

$$\frac{(1 + \gamma L) [\rho_{v,\infty}]_{x=0} + [\rho_{v,\infty}]_{x=L}}{\gamma l + 2} + \rho_{v,tr}(0, t)$$

$$\rho_v(L, t) = \rho_{v,st}(L) + \rho_{v,tr}(L, t) = \quad (9.15)$$

$$\frac{(1 + \gamma L) [\rho_{v,\infty}]_{x=L} + [\rho_{v,\infty}]_{x=0}}{\gamma l + 2} + \rho_{v,tr}(L, t)$$

The transient (homogenous) problem is given by

$$\frac{\partial \rho_{v,tr}}{\partial t} - \alpha \frac{\partial^2 \rho_{v,tr}}{x^2} = 0, \quad 0 < x < L, \quad t > 0, \quad \alpha = \frac{D_v}{\varepsilon + \rho_s f'(\rho_v)} \quad (9.16)$$

$$\left. \frac{\partial \rho_{v,tr}}{\partial x} \right|_{x=0} - \gamma \rho_{v,tr}(0, t) = 0, \quad \left. \frac{\partial \rho_{v,tr}}{\partial x} \right|_{x=L} + \gamma \rho_{v,tr}(L, t) = 0, \quad t > 0 \quad (9.17)$$

$$\rho_{v,tr}(x, 0) = \rho_v(x, 0) - \rho_{v,st}(x), \quad 0 < x < L \quad (9.18)$$

Variable separation

$$\rho_{v,tr} = X(x)T(t) \quad (9.19)$$

Differentiate (9.19) and insert into the differential equation (9.16)

$$\frac{1}{\alpha T} \frac{dT}{dt} = \frac{1}{X} \frac{d^2 X}{dx^2} \quad (9.20)$$

Assign the terms in (9.20) constant values $-\beta^2$

$$\left. \begin{aligned} \frac{dT}{dt} + \alpha \beta^2 T &= 0 \\ \frac{d^2 X}{dx^2} + \beta^2 X &= 0 \end{aligned} \right\} \begin{aligned} T &= c_1 e^{-\alpha \beta^2 t} \\ X &= c_2 \cos(\beta x) + c_3 \sin(\beta x) \end{aligned} \quad (9.21)$$

(9.21) inserted into (9.19) gives the solution

$$\rho_{v,tr} = (A \cos(\beta x) + B \sin(\beta x)) e^{-\alpha \beta^2 t} \quad (9.22)$$

Insertion of boundary conditions (9.17) into (9.22) results in

$$B\beta - A\gamma = 0 \quad (9.23)$$

$$-A\beta\sin(\beta L) + B\beta\cos(\beta L) + A\gamma\cos(\beta L) + B\gamma\sin(\beta L) = 0 \quad (9.24)$$

Rearrangement of (9.23) and (9.24) results in

$$\tan(\beta L) = \frac{2\gamma\beta}{\beta^2 - \gamma^2} \quad (9.25)$$

or

$$2\cot(a) = \frac{a}{\gamma L} - \frac{\gamma L}{a}, \quad a = \beta L \quad (9.26)$$

(9.26) has an infinite number of positive (and negative) roots in the intervals

$$I_k = \pm\{(k-1)\pi \quad k\pi\}, \quad k = 1, 2, \dots \quad (9.27)$$

Boundary conditions together with roots give the solution

$$\rho_{v,tr}^k = A_k(\cos(\beta_k x) + \frac{\gamma}{\beta_k}\sin(\beta_k x))e^{-\alpha\beta_k^2 t} = A_k\varphi_k e^{-\alpha\beta_k^2 t} \quad (9.28)$$

$$\rho_{v,tr} = \sum_{k=1}^{\infty} A_k\varphi_k(x)e^{-\alpha\beta_k^2 t} \quad (9.29)$$

where $\varphi_k(x)$ constitutes an orthogonal basis, i.e.

$$\langle \varphi_k | \varphi_l \rangle = 0, \quad k \neq l \quad (9.30)$$

Equation (9.18) and inserting $t = 0$ in (9.29) result in

$$\rho_{v,tr}(x, 0) = \sum_{k=1}^{\infty} A_k\varphi_k(x) = \rho_v(x, 0) - \rho_{v,st}(x)$$

Develop $\rho_v(x, 0) - \rho_{v,st}$ in the above given series, i.e. A_k becomes

$$A_k = \frac{\langle \rho_v(x, 0) - \rho_{v,st} | \varphi_k \rangle}{\langle \varphi_k | \varphi_k \rangle} = \frac{\int_0^L (\rho_v(x, 0) - \rho_{v,st})\varphi_k dx}{\int_0^L \varphi_k^2 dx} \quad (9.31)$$

Total solution is given by

$$\rho_v(x, t) = \rho_{v,st}(x) + \sum_{k=1}^{\infty} A_k \varphi_k(x) e^{-\alpha \beta_k^2 t} \quad (9.32)$$

A_k from (1.31) is generally expressed as

$$\begin{aligned} A_k = & -2 \left[-\rho_v(x, 0) \gamma L \sin(L\beta_k) \beta_k^2 - \gamma^2 [\rho_{v,\infty}]_{x=L} \beta_k \cos(L\beta_k) L + \right. \\ & \rho_v(x, 0) \gamma^2 L \cos(L\beta_k) \beta_k - 2\gamma [\rho_{v,\infty}]_{x=0} \cos(L\beta_k) \beta_k - 2\rho_v(x, 0) \sin(L\beta_k) \beta_k^2 + \\ & \gamma [\rho_{v,\infty}]_{x=L} \beta_k^2 \sin(L\beta_k) L + 2\rho_v(x, 0) \gamma \cos(L\beta_k) \beta_k + \gamma^2 [\rho_{v,\infty}]_{x=L} \sin(L\beta_k) + \\ & [\rho_{v,\infty}]_{x=L} \sin(L\beta_k) \beta_k^2 + [\rho_{v,\infty}]_{x=0} \sin(L\beta_k) \beta_k^2 - \gamma^2 [\rho_{v,\infty}]_{x=0} \sin(L\beta_k) - \\ & \left. \rho_v(x, 0) \gamma^2 L \beta_k - 2\rho_v(x, 0) \gamma \beta_k + \gamma^2 [\rho_{v,\infty}]_{x=0} L \beta_k + 2\gamma [\rho_{v,\infty}]_{x=0} \beta_k \right] / \\ & \left[(\gamma L + 2) (\cos(L\beta_k) \sin(L\beta_k) \beta_k^2 + L \beta_k^3 - 2\gamma \cos(L\beta_k)^2 \beta_k - \gamma^2 \cos(L\beta_k) \right. \\ & \left. \sin(L\beta_k) + \gamma^2 \beta_k L + 2\gamma \beta_k) \right] \quad (9.33) \end{aligned}$$

Appendix D

Element functions

```
function C_ap=moist2i4e_C_ap(ex,ey,e,h)
%-----
% PURPOSE
% Compute contribution C_ap to element conductivity
% matrix for 4 node isoparametric field element
%-----
% INPUT:  ex = [x1 x2 x3 x4]   element coordinates
%         ey = [y1 y2 y3 y4]
%         e           porosity
%         h           thickness
%-----
% OUTPUT: C_ap : element 'conductivity' matrix (8 x 8)
%-----
% Copyright (c) Division of Structural Mechanics and
%                Department of Solid Mechanics.
%                Lund Institute of Technology
%-----

%Gauss points coordinates
ir=2;
ngp=ir*ir;
g1=0.577350269189626;
gp(:,1)=[-g1; g1; g1; -g1]; gp(:,2)=[-g1;-g1; g1; g1];
xsi=gp(:,1); eta=gp(:,2); r2=ngp*2;

%Shape functions
N=zeros(ngp,8);
N1=(1-xsi).*(1-eta)/4; N2=(1+xsi).*(1-eta)/4;
N3=(1+xsi).*(1+eta)/4; N4=(1-xsi).*(1+eta)/4;
N(:,[1:2:7])=[N1 N2 N3 N4];
```



```

%Shape gradients
dNr(1:2:r2,1)=-(1-eta)/4;    dNr(1:2:r2,2)= (1-eta)/4;
dNr(1:2:r2,3)= (1+eta)/4;    dNr(1:2:r2,4)=- (1+eta)/4;
dNr(2:2:r2+1,1)=-(1-xsi)/4;  dNr(2:2:r2+1,2)=- (1+xsi)/4;
dNr(2:2:r2+1,3)= (1+xsi)/4;  dNr(2:2:r2+1,4)= (1-xsi)/4;

%Integration
C_ap=zeros(8,8);
JT=dNr*[ex;ey]';
for i=1:ngp
    indx=[ 2*i-1; 2*i ];
    detJ=det(JT(indx,:));
    if detJ<10*eps
        disp('Jacobideterminanten lika med noll!')
    end
    JTinv=inv(JT(indx,:));
    C_ap=C_ap+N(i,:)'*N(i,)*detJ;
end

C_ap=C_ap*e*h;
%-----end C_ap-----

```

```

function [K_ai,Q_ai]=moist2i4e_K_ai_Q_ai(ex,ey,rho,kc,h,dc,c)
%-----
% PURPOSE
% Compute contribution K_ai to element stiffness
% matrix and Q_ai to the element residual vector
% for 4 node isoparametric field element
%-----
% INPUT:  ex = [x1 x2 x3 x4]           element coordinates
%         ey = [y1 y2 y3 y4]
%         rho                density
%         kc                 intra-fiber mass
%                           transport coefficient
%         h                  thickness
%         dc=[dc1 dc2 dc3 dc4]       slope of equilibrium
%                                   moisture concentration
%         c=[c1 c2 c3 c4]           equilibrium moisture concentration
%-----
% OUTPUT: K_ai : element 'stiffness' matrix (8 x 8)
%         Q_ai : contribute to residual vector (8 x 1)
%-----
% Copyright (c) Division of Structural Mechanics and
%                Department of Solid Mechanics.
%                Lund Institute of Technology
%-----

%Gauss points coordinates
ir=2;
ngp=ir*ir;
g1=0.577350269189626;
gp(:,1)=[-g1; g1;g1; -g1]; gp(:,2)=[-g1;-g1; g1; g1];
xsi=gp(:,1); eta=gp(:,2); r2=ngp*2;

%Shape functions
N=zeros(ngp,8);
N1=(1-xsi).*(1-eta)/4; N2=(1+xsi).*(1-eta)/4;
N3=(1+xsi).*(1+eta)/4; N4=(1-xsi).*(1+eta)/4;
N(:,[1:2:7])=[N1 N2 N3 N4];

%Shape gradients
dNr(1:2:r2,1)=- (1-eta)/4;   dNr(1:2:r2,2)= (1-eta)/4;
dNr(1:2:r2,3)= (1+eta)/4;   dNr(1:2:r2,4)=- (1+eta)/4;
dNr(2:2:r2+1,1)=- (1-xsi)/4; dNr(2:2:r2+1,2)=- (1+xsi)/4;
dNr(2:2:r2+1,3)= (1+xsi)/4; dNr(2:2:r2+1,4)= (1-xsi)/4;

```

```

%Integration
K_ai=zeros(8,8);
Q_ai=zeros(8,1);
JT=dNr*[ex;ey]';
for i=1:ngp
    dcg=N1(i)*dc(1)+N2(i)*dc(2)+N3(i)*dc(3)+N4(i)*dc(4);
    cg=N1(i)*c(1)+N2(i)*c(2)+N3(i)*c(3)+N4(i)*c(4);
    indx=[ 2*i-1; 2*i ];
    detJ=det(JT(indx,:));
    if detJ<10*eps
        disp('Jacobideterminanten lika med noll!')
    end
    JTinv=inv(JT(indx,:));
    K_ai=K_ai+N(i,:)'*N(i,:)*detJ*dcg;
    Q_ai=Q_ai+N(i,:)'*detJ*cg;
end

K_ai=K_ai*rho*h*kc;
Q_ai=-Q_ai*rho*h*kc;
%-----end K_ai,Q_ai-----

```

```

function K_ac=moist2i4e_K_ac(ex,ey,rho,h,kc)
%-----
% PURPOSE
% Compute contribution K_ac to element stiffness
% matrix for 4 node isoparametric field element
%-----
% INPUT:  ex = [x1 x2 x3 x4]   element coordinates
%         ey = [y1 y2 y3 y4]
%         kc                intra-fibre mass transfer
%                           coefficient
%         rho                density
%         h                  thickness
%-----
% OUTPUT: K_ac : element 'stiffness' matrix (8 x 8)
%-----
% Copyright (c) Division of Structural Mechanics and
%                Department of Solid Mechanics.
%                Lund Institute of Technology
%-----

%Gauss points coordinates
ir=2;
ngp=ir*ir;
g1=0.577350269189626;
gp(:,1)=[-g1; g1; g1; -g1]; gp(:,2)=[-g1;-g1; g1; g1];
xsi=gp(:,1); eta=gp(:,2); r2=ngp*2;

%Shape functions
Na=zeros(ngp,8);
Nb=zeros(ngp,8);
N1=(1-xsi).*(1-eta)/4; N2=(1+xsi).*(1-eta)/4;
N3=(1+xsi).*(1+eta)/4; N4=(1-xsi).*(1+eta)/4;
Na(:, [1:2:7])=[N1 N2 N3 N4];
Nb(:, [2:2:8])=[N1 N2 N3 N4];

%Shape gradients
dNr(1:2:r2,1)=- (1-eta)/4;   dNr(1:2:r2,2)= (1-eta)/4;
dNr(1:2:r2,3)= (1+eta)/4;   dNr(1:2:r2,4)=- (1+eta)/4;
dNr(2:2:r2+1,1)=- (1-xsi)/4; dNr(2:2:r2+1,2)=- (1+xsi)/4;
dNr(2:2:r2+1,3)= (1+xsi)/4; dNr(2:2:r2+1,4)= (1-xsi)/4;

%Integration
K_ac=zeros(8,8);
JT=dNr*[ex;ey]';

```

```
for i=1:ngp
    indx=[ 2*i-1; 2*i ];
    detJ=det(JT(indx,:));
    if detJ<10*eps
        disp('Jacobideterminanten lika med noll!')
    end
    JTinv=inv(JT(indx,:));
    K_ac=K_ac+Na(i,:)'*Nb(i,:)*detJ;
end

K_ac=-K_ac*rho*h*kc;
%-----end K_ac-----
```

```

function K_dA=moist2i4e_K_dA(ex,ey,h,kb,boundary_nodes)
%-----
% PURPOSE
% Compute contribution K_dA to element stiffness
% matrix for 4 node (isoparametric) boundary element
%-----
% INPUT:  ex = [x1 x2 x3 x4]   element coordinates
%         ey = [y1 y2 y3 y4]
%         h           thickness
%         kb          boundary convection coefficient
%
%         boundary_nodes      nodes specifying each convective
%                             boarderline in the element
%                             [nbr of boarderlines x 2]
%-----
% OUTPUT: K_dA : element 'stiffness' matrix (8 x 8)
%-----
% Copyright (c) Division of Structural Mechanics and
%                Department of Solid Mechanics.
%                Lund Institute of Technology
%-----

%Integration
K_dA=zeros(8,8);
for i=1:length(boundary_nodes(:,1))
    delta_x=(ex(boundary_nodes(i,1))-ex(boundary_nodes(i,2)));
    delta_y=(ey(boundary_nodes(i,1))-ey(boundary_nodes(i,2)));
    L=sqrt(delta_x^2+delta_y^2);

    K_dA(boundary_nodes(i,1)*2-1,boundary_nodes(i,1)*2-1)=2;
    K_dA(boundary_nodes(i,2)*2-1,boundary_nodes(i,2)*2-1)=2;
    K_dA(boundary_nodes(i,1)*2-1,boundary_nodes(i,2)*2-1)=1;
    K_dA(boundary_nodes(i,2)*2-1,boundary_nodes(i,1)*2-1)=1;
end

K_dA=K_dA*h*kb*L/6;
%-----end K_dA-----

```

```

function K_av=moist2i4e_K_av(ex,ey,Dv,h)
%-----
% PURPOSE
% Compute contribution K_av to element stiffness
% matrix for 4 node isoparametric field element
%-----
% INPUT:  ex = [x1 x2 x3 x4]   element coordinates
%         ey = [y1 y2 y3 y4]
%
%         Dv           diffusivity in the pores
%         h            thickness
%-----
% OUTPUT: K_av : element 'stiffness' matrix (8 x 8)
%-----
% Copyright (c) Division of Structural Mechanics and
%                Department of Solid Mechanics.
%                Lund Institute of Technology
%-----

%Gauss points coordinates
ir=2;
ngp=ir*ir;
g1=0.577350269189626;
gp(:,1)=[-g1; g1; g1; -g1]; gp(:,2)=[-g1;-g1; g1; g1];
xsi=gp(:,1); eta=gp(:,2); r2=ngp*2;

%Shape functions
N=zeros(ngp,8);
N1=(1-xsi).*(1-eta)/4; N2=(1+xsi).*(1-eta)/4;
N3=(1+xsi).*(1+eta)/4; N4=(1-xsi).*(1+eta)/4;
N(:,[1:2:7])=[N1 N2 N3 N4];

%Shape gradients
dNr(1:2:r2,1)=- (1-eta)/4;   dNr(1:2:r2,2)= (1-eta)/4;
dNr(1:2:r2,3)= (1+eta)/4;   dNr(1:2:r2,4)=- (1+eta)/4;
dNr(2:2:r2+1,1)=- (1-xsi)/4; dNr(2:2:r2+1,2)=- (1+xsi)/4;
dNr(2:2:r2+1,3)= (1+xsi)/4; dNr(2:2:r2+1,4)= (1-xsi)/4;

%Integration
K_av=zeros(8,8);
JT=dNr*[ex;ey]';
D=[Dv 0;0 Dv];
for i=1:ngp
    indx=[ 2*i-1; 2*i ];

```

```
detJ=det(JT(indx,:));
if detJ<10*eps
    disp('Jacobideterminanten lika med noll!')
end
JTinv=inv(JT(indx,:));
B=JTinv*dNr(indx,:);
K_av([1 3 5 7],[1 3 5 7])=K_av([1 3 5 7],[1 3 5 7])+B'*D*B*detJ;
end

K_av=K_av*h;
%-----end K_av-----
```



```

function C_bc=moist2i4e_C_bc(ex,ey,h)
%-----
% PURPOSE
% Compute contribution C_bc to element conductivity
% matrix for 4 node isoparametric field element
%-----
% INPUT:  ex = [x1 x2 x3 x4]   element coordinates
%         ey = [y1 y2 y3 y4]
%         h   thickness
%-----
% OUTPUT: C_bc : element 'conductivity' matrix (8 x 8)
%-----
% Copyright (c) Division of Structural Mechanics and
%                Department of Solid Mechanics.
%                Lund Institute of Technology
%-----

%Gauss points coordinates
ir=2;
ngp=ir*ir;
g1=0.577350269189626;
gp(:,1)=[-g1; g1;-g1; g1]; gp(:,2)=[-g1;-g1; g1; g1];
xsi=gp(:,1); eta=gp(:,2); r2=ngp*2;

%Shape functions
N=zeros(ngp,8);
N1=(1-xsi).*(1-eta)/4; N2=(1+xsi).*(1-eta)/4;
N3=(1+xsi).*(1+eta)/4; N4=(1-xsi).*(1+eta)/4;
N(:, [2:2:8])=[N1 N2 N3 N4];

%Shape gradients
dNr(1:2:r2,1)=- (1-eta)/4;   dNr(1:2:r2,2)= (1-eta)/4;
dNr(1:2:r2,3)= (1+eta)/4;   dNr(1:2:r2,4)=- (1+eta)/4;
dNr(2:2:r2+1,1)=- (1-xsi)/4; dNr(2:2:r2+1,2)=- (1+xsi)/4;
dNr(2:2:r2+1,3)= (1+xsi)/4; dNr(2:2:r2+1,4)= (1-xsi)/4;

%Integration
C_bc=zeros(8,8);
JT=dNr*[ex;ey]';
for i=1:ngp
    indx=[ 2*i-1; 2*i ];
    detJ=det(JT(indx,:));
    if detJ<10*eps
        disp('Jacobideterminanten lika med noll!')
```

```
    end
    JTinv=inv(JT(indx,:));
    C_bc=C_bc+N(i,:)'*N(i,)*detJ;
end

C_bc=C_bc*h;
%-----end C_bc-----
```

```

function [K_bi,Q_bi]=moist2i4e_K_bi_Q_bi(ex,ey,c,dc,h,kc)
%-----
% PURPOSE
% Compute contribution K_bi to element stiffness
% and Q_bi to the element residual vector
% for 4 node isoparametric field element
%-----
% INPUT:  ex = [x1 x2 x3 x4]           element coordinates
%         ey = [y1 y2 y3 y4]
%         dc=[dc1 dc2 dc3 dc4]       slope of equilibrium
%                                     moisture concentration
%         c=[c1 c2 c3 c4]           equilibrium moisture concentration
%         h                                     thickness
%         kc                                     intra-fibre mass transfer
%-----
% OUTPUT: K_bi : element 'stiffness' matrix (8 x 8)
%         Q_bi : element 'residual' vector (8 x 1)
%-----
% Copyright (c) Division of Structural Mechanics and
%                 Department of Solid Mechanics.
%                 Lund Institute of Technology
%-----

%Gauss points coordinates
ir=2;
ngp=ir*ir;
g1=0.577350269189626; w1=1;
gp(:,1)=[-g1; g1;g1; -g1]; gp(:,2)=[-g1;-g1; g1; g1];
xsi=gp(:,1); eta=gp(:,2); r2=ngp*2;

%Shape functions
Na=zeros(ngp,8);
Nb=zeros(ngp,8);
N1=(1-xsi).*(1-eta)/4; N2=(1+xsi).*(1-eta)/4;
N3=(1+xsi).*(1+eta)/4; N4=(1-xsi).*(1+eta)/4;
Na(:,[1:2:7])=[N1 N2 N3 N4];
Nb(:,[2:2:8])=[N1 N2 N3 N4];

%Shape gradients
dNr(1:2:r2,1)=- (1-eta)/4;   dNr(1:2:r2,2)= (1-eta)/4;
dNr(1:2:r2,3)= (1+eta)/4;   dNr(1:2:r2,4)=- (1+eta)/4;
dNr(2:2:r2+1,1)=- (1-xsi)/4; dNr(2:2:r2+1,2)=- (1+xsi)/4;
dNr(2:2:r2+1,3)= (1+xsi)/4; dNr(2:2:r2+1,4)= (1-xsi)/4;

```

```

%Integration
K_bi=zeros(8,8);
Q_bi=zeros(8,1);
JT=dNr*[ex;ey]';
for i=1:ngp
    dcg=N1(i)*dc(1)+N2(i)*dc(2)+N3(i)*dc(3)+N4(i)*dc(4);
    cg=N1(i)*c(1)+N2(i)*c(2)+N3(i)*c(3)+N4(i)*c(4);
    indx=[ 2*i-1; 2*i ];
    detJ=det(JT(indx,:));
    if detJ<10*eps
        disp('Jacobideterminanten lika med noll!')
    end
    JTinv=inv(JT(indx,:));
    K_bi=K_bi+Nb(i,:)'*Na(i,:)*detJ*dcg;
    Q_bi=Q_bi+Nb(i,:)'*detJ*cg;
end

K_bi=-K_bi*h*kc;
Q_bi=Q_bi*h*kc;
%-----end K_bi,Q_bi-----

```

```

function K_bc=moist2i4e_K_bc(ex,ey,kc,h)
%-----
% PURPOSE
% Compute contribution K_bc to element stiffness
% matrix for 4 node isoparametric field element
%-----
% INPUT:  ex = [x1 x2 x3 x4]   element coordinates
%         ey = [y1 y2 y3 y4]
%         kc                intra-fibre mass transfer
%                           coefficient
%         h                  thickness
%-----
% OUTPUT: K_bc : element 'stiffness' matrix (8 x 8)
%-----
% Copyright (c) Division of Structural Mechanics and
%                Department of Solid Mechanics.
%                Lund Institute of Technology
%-----

%Gauss points coordinates
ir=2;
ngp=ir*ir;
g1=0.577350269189626;
gp(:,1)=[-g1; g1;-g1; g1]; gp(:,2)=[-g1;-g1; g1; g1];
xsi=gp(:,1); eta=gp(:,2); r2=ngp*2;

%Shape functions
N=zeros(ngp,8);
N1=(1-xsi).*(1-eta)/4; N2=(1+xsi).*(1-eta)/4;
N3=(1+xsi).*(1+eta)/4; N4=(1-xsi).*(1+eta)/4;
N(:, [2:2:8])=[N1 N2 N3 N4];

%Shape gradients
dNr(1:2:r2,1)=- (1-eta)/4;   dNr(1:2:r2,2)= (1-eta)/4;
dNr(1:2:r2,3)= (1+eta)/4;   dNr(1:2:r2,4)=- (1+eta)/4;
dNr(2:2:r2+1,1)=- (1-xsi)/4; dNr(2:2:r2+1,2)=- (1+xsi)/4;
dNr(2:2:r2+1,3)= (1+xsi)/4; dNr(2:2:r2+1,4)= (1-xsi)/4;

%Integration
K_bc=zeros(8,8);
JT=dNr*[ex;ey]';
for i=1:ngp
    indx=[ 2*i-1; 2*i ];
    detJ=det(JT(indx,:));

```

```
if detJ<10*eps
    disp('Jacobideterminanten lika med noll!')
end
JTinv=inv(JT(indx,:));
K_bc=K_bc+N(i,:)'*N(i,)*detJ;
end

K_bc=K_bc*kc*h;
%-----end K_bc-----
```